UNIVERSITY OF CALIFORNIA SAN DIEGO

Toward Commercial Perovskite Solar Manufacturing

A Thesis submitted in partial satisfaction of the requirements for the degree of Master of Science

in

Chemical Engineering

by

Zachary Dorfman

Committee in charge:

Professor David P. Fenning, Chair
Professor Darren Lipomi
Professor Ping Liu

2019

This Thesis of Zachary Dorfman is approved, and it is acceptable in quality and form for publication on microfilm and electronically:

_____

_____

_____
Chair

University of California San Diego

2019

TABLE OF CONTENTS

LIST OF FIGURES

AKNOWLEDGMENTS

Family. First and foremost, to my parents and family; Thank you. Mom and Dad, there are no words that can express the amount of gratitude and love I have for you two. You created something so amazing from practically nothing, and I am so fortunate to be your son. Max and Sam, you guys are the greatest little brothers I could have asked for. I know I can count on either of you for anything, and I know you feel the same of me. Brian and Wendy, I couldn't have asked for a better aunt and uncle. You two are so much fun to hang out and talk to, Braiden and Carson don't know how lucky they are. B you're a smart kid, but just remember you'll never be able to beat me in Catan. Cus, I'm still not sorry for missing your birthday.

The Fenning Group. David, I am truly grateful for your mentorship and the opportunity to work for you. At times I didn't know what the next steps were, and your guidance motivated me to persevere. Yanqi (Grace) Luo, I remember the day I made my first solar cells with you, joking about setting the world record while you reassured me that I wasn't getting above 1% PCE; you were right. Thank you for all your help, any group will be lucky to have you as a post-doc. To the rest of the SOLEIL group: Rishi, Taewoo, Moses, Xueying (Sherry), Guillaume, Eric, and Manas; Thank you. All of you have provided me with support at one time or another. The future of the Fenning laboratory is in great hands.

Collaborators. Thank you to the Lipomi Group and Rory Runser for continuous use of their facilities and training. Thank you Nano3 for supplying a shared facility space for UCSD graduate students to regularly conduct high level research.

ABSTRACT OF THE THESIS

Toward Commercial Perovskite Solar Manufacturing

by

Zachary Dorfman

Master of Science in Chemical Engineering

University of California San Diego, 2019

Professor David P. Fenning, Chair

Hybrid perovskite solar cells (PSCs) have received considerable attention in the hopes of a paradigm shift towards low-cost, high-efficiency light energy harvesting. In just a decade, researchers have increased the record certified power conversion efficiency (PCE) of perovskite solar cells (PSCs) from 3.8% to a record 23.3%. Much of this research has been conducted in lab-scale settings. However, to compete in the current energy sector, solutions to large-scale,

cost-effective manufacturing must be engineered. Recent progress from various groups have presented viable solutions to scaled perovskite synthesis, often focusing on the absorber layer, while neglecting other necessary layers. An integral part of PSCs are electron transport layers (ETLs). ETLs serve as an electron selective barrier at the cathode and facilitate the ability to extract high currents. To date, the large-area PSC community has systematically researched scalability with insufficient reports on transport layer commercialization, specifically SnO_2 ETL industrial manufacturability. Vacuum thermal evaporation can reproducibly deposit high purity thin films, over large areas, at high volume. Combined with ease of automation, it is a highly compatible technique for assembly-line manufacturing. Herein, we report the use of vacuum thermally evaporated (vte) SnO_2 ETLs to produce stable and efficient PSCs. The fabricated vte-SnO_2 ETLs excellent coverage, confirmed through cyclic voltammetry, on substrates ranging from 5 cm^2 up to 100 cm^2. Additionally, PSC devices fabricated with VTE-SnO_2 ETLs on average display slightly higher PCE, ~16%, than our standard solution processed SnO_2 ETLs, ~15.7%. These results help pave the way for commercial manufacturing of perovskite solar modules.

Chapter 1

Motivation and Scope of Thesis

Modern civilization is entirely based on human kind's capacity to efficiently capture and convert energy into usable forms. Harvesting fossil fuels has managed to get us pretty far, but without a transition to sustainable energy we are in the face a serious supply-demand problem.[1] Energy demands are continuously growing as the population continues to rise. In just a hundred years, between 1900 and 2000, the world's population jumped from 1.5 to 6.1 billion people, while our fossil fuel resources are depleted orders of magnitude faster than they can be regenerated.[2] Fortunately, the sun supplies the earth with more energy per day than the present population consumes during a whole year. Until we discover efficient methods to produce nuclear fusion or safer forms of fission power, the sun is by far our greatest source of energy. Over the past few decades, significant efforts have been made to improve our ability to harvest sunlight energy. However, at a more fundamental level, the ability to efficiently convert this abundant energy resource still remains a significant problem. In an ideal world, solar cells would have high power conversion efficiency (PCE) over long periods of time at low manufacturing cost. Unfortunately, this has not been the case, forcing tradeoffs in costs and efficiencies.[1,2]

In 2011, the Department of Energy (DOE) launched the SunShot initiative with the goal to reduce the cost of solar energy and making it a competitive energy source with fossil fuels.[3] This effort resulted in the development of many new PV technologies based on cheap materials and low-cost processes, however, only one produces high enough efficiencies for commercial market penetration, perovskite solar cells (PSCs). A PSC utilizes a solution processed organic-inorganic lead halide semiconductor that serves as the semiconducting light absorber. This

material has generated a lot of excitement and in just a decade, researchers have increased the record certified PCE from 3.8% to a record 23.3%.[4] This incredible advancement can majorly be attributed perovskite's excellent optoelectronic properties such as tunable direct band gap, high absorption coefficient, and excellent charge carrier mobility. Compared to conventional silicon solar cells that require large costly manufacture facilitates, PSCs can be fabricated through commonplace wet chemistry methods at extremely low cost.

This thesis aims to play a role in advancing the commercialization of PSCs through studying and scaling the auxiliary layers that essential for high current extraction. The work presented in the results and discussions sections serve to establish two main points. Firstly, that vacuum thermal evaporation is an efficient technique for commercially scaling SnO_2 electron transport layer manufacturing. Additionally, it is a better alternative to other scalable methods based on its assembly-line compatibility, high reproducibility, and practically zero percent waste production. Secondly, insight on conduction band tailoring in wide band gap semiconducting metal oxides is looked into through mixed ZnO-SnO_2 (ZTO) ALD layers for potential photovoltaic application. Through CB tailoring, a useful relationship is established potentially enabling the ability to optimize device V_{oc} through ETL characterization without full device fabrication. The option to tune and test ETL conditions to maximize PCE values without having to fabricate a full PSC would save a great deal of time or resources.

Chapter 2

General and Physical Background

2.1 Atomic Orbitals, Molecular Orbitals, and Band Formation

Development of the atomic model is a constantly evolving pursuit to describe electron-nuclear interactions. In 1913 Niels Bohr proposed a classical model, stating that electrons were analogous to that of celestial bodies with fixed orbits corresponding to discrete energy values. The true nature of the electron is quite complex and is currently described with a quantum mechanical view. Like the uncertainty principles says, we can never truly define an electron's location or movement with certainty: we can only describe an electrons position and energy through probabilities. The current model states that atomic orbitals (AOs) describe a volume of space wherein there is a high probability of finding an electron.[5] The shape and energy of these AOs expressed with quantum number notation, depicted in Figure 2.1.

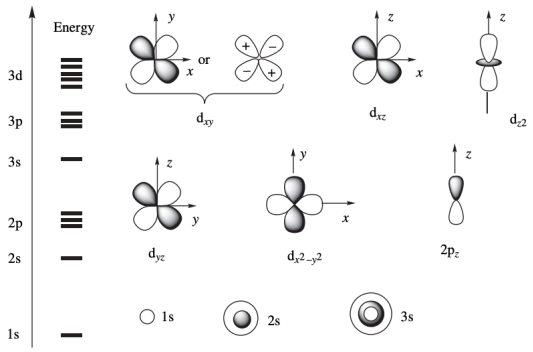

Figure 2.1: Approximate shapes and energies of a few atomic orbitals.[5]

The principle quantum number (n) relates the size of the orbital, with $n = 1$ describing the lowest energy orbital containing the most tightly bound electrons. The angular momentum quantum number (l) determines the shape and angular distribution of the orbital. Although l takes

on integer values, it is usually expressed by the letters s, p, d, f. These "distinct" orbitals are actually reflections of the probability of finding an electron in that region of space.[6]

As atoms come together to form molecule, their individual orbitals overlap to form molecular orbitals (MOs). This well-known phenomenon, bonding, results from atoms sharing electrons. The outer unfilled orbitals, valence orbitals, contain the electrons in that partake in bonding. Bonding orbitals split into bonding and anti-bonding states due to interference and the wavelike nature of electrons. Bonding orbitals result from a high electron density between two nuclei, shielding nuclear Coulombic repulsion and lowering the overall energy relative to the individual atoms. In contrast, electrons that do not partake in bonding raise the energy of the system and form anti-bonding states, which destabilize the structure. Therefore, electrons will elect to occupy stable binding states first and then proceed to anti-binding orbitals. A basic example of this is that two hydrogen atoms will come together to form H_2, but helium will not form He_2. As molecules are formed, the ammount of orbitals split proportional to number of atoms in the molecule.[5,7] One can see that tracking MOs can get complicated quickly just by looking at the depiction of a simple ethane molecule in Figure 2.2b.

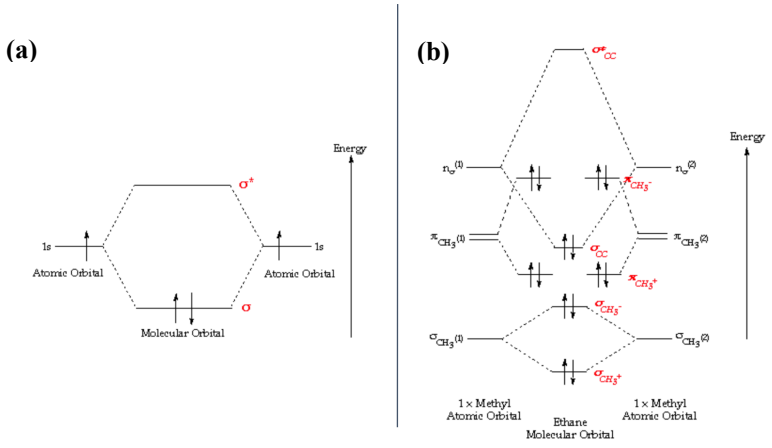

Figure 2.2: Molecular orbitals for a **(a)** H_2 molecule and an **(b)** ethane molecule.[7]

As increasing numbers of atoms come together to form solids, the number of MOs becomes exceedingly large and the energy between them becomes vanishingly small. The difference between valence orbital energies becomes indistinguishable and can no longer be assigned to individual atoms. The once discrete bonding orbitals now form a continuum of allowed energy states forming the valence band (VB). The higher energy anti-bonding orbitals merge in the same manner to form the conduction band (CB). This is the Band Theory of solids and is useful way of visualizing the available energy states for electrons and essential for the subsequent discussion on semiconductors.[5,7,8]

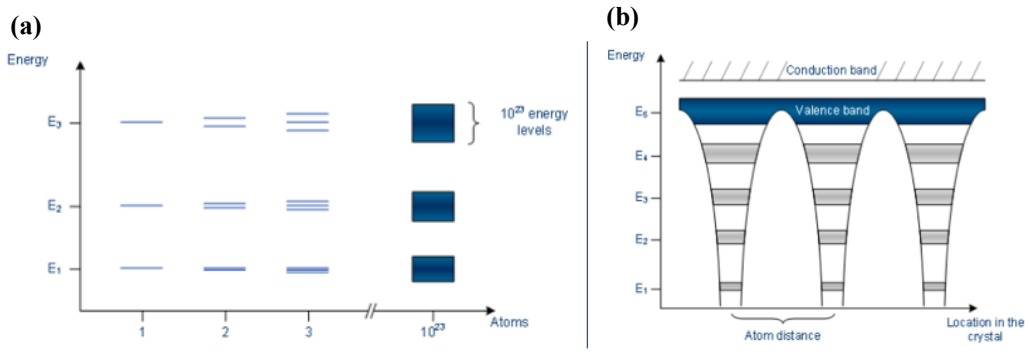

Figure 2.3: (a) Illustration of discrete energy states becoming indistinguishable and **(b)** forming continuous energy bands.[8]

2.2 Important Semiconductor Concepts for Photovoltaics

2.2.1 Band Gap

Solid materials are classified into three main groups based upon their electronic behavior: insulators, semiconductors, and conductors. As previously mentioned, solids contain a VB and CB which describe the allowed energy states electrons can occupy in a solid. The VB contains the atoms' outermost electrons used to form the structure and the CB consists of higher energy states that electrons don't typically occupy. Electrons in the CB have the ability to move freely

through the solid's band structure between neighboring atoms. The energy distance between the VB and CB is a called a bandgap (E_g). By definition, E_g is the energy gap between the bound state and the free state, and is the minimum energy required to excite an electron to a state of conduction. In metals, electrons move freely through the structure because there is essentially no E_g, which is why metals are good conductors. Insulators have a large E_g, which is why they are bad conductors of electricity. Semiconductors are the interesting class of materials that behave as insulators normally but have the ability to operate as conductors.[1,7,8]

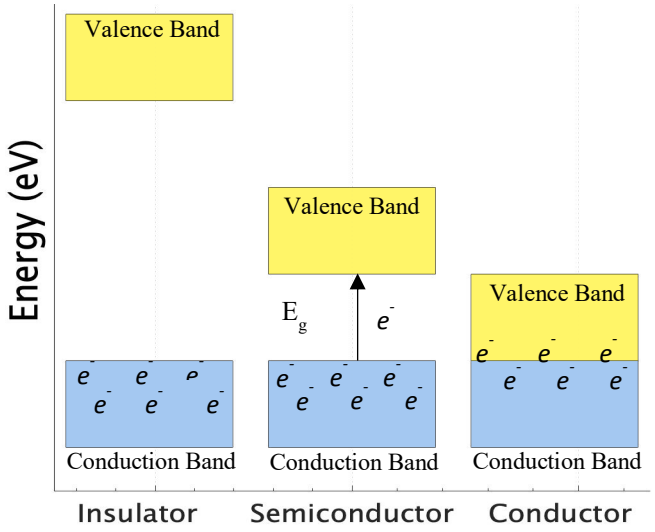

Figure 2.4: Illustration of band gap differences for insulators, semiconductors, and conductors.

2.2.2 Charge Carriers

When electrons get promoted to the CB, they become free to participate in conduction and leave behind a void in the VB called a "hole". These holes are not necessarily real particles; however, it is extremely useful to treat them as such. Defining the empty VB states as particles makes it much easier to conceptualize and calculate interactions between and the crystal's incomplete lattice and the electrons. Moreover, the ability to this is based on the fact that holes

in the VB behave extremely similar to electrons in the CB. They are charged, have an effective mass, and participate in conduction. Consequently, the electrons and holes in semiconductors are referred to as "charge carriers".[1,8,9]

2.2.3 Fermi Energy and Carrier Concentration

The operation of any semiconductor device inherently depends on its concentration of charge carriers. As the name implies, charge carriers transport charge and are the source of electrical currents. In order to understand PV device operation, it is important to know how charge carrier concentrations are calculated and the impact they have on a semiconductors electronic structure. To determine the carrier concentration we require two functions, the density of states (DOS) function, $g(E)$, and the occupation function, $f(E)$. The DOS describes the number of allowable energy states per unit of volume. Adequate calculations in semiconductors require two equations corresponding to the DOS in the CB and the VB, excluding the range of forbidden energies in the E_g.[1]

$$g_c(E) = \left(\frac{\sqrt{8}\,\pi\, m_n^*}{h^3}\right)^{\frac{3}{2}} * \sqrt{E - E_{CB}}\,, \quad for \;\; E \geq E_{CB} \qquad \textbf{(1)}$$

$$g_v(E) = \left(\frac{\sqrt{8}\,\pi\, m_p^*}{h^3}\right)^{\frac{3}{2}} * \sqrt{E_{VB} - E}\,, \quad for \;\; E \leq E_{VB} \qquad \textbf{(2)}$$

Where m_n^* and m_p^* are the electron and hole effective masses, respectively, and represent the particles apparent mass in response to external forces or interactions. The occupation function is the famous Fermi-Dirac distribution function and describes the ratio of electron filled states to the total allowed states at a given energy.[1,9]

$$f(E) = \frac{1}{1+exp\left(\frac{E-E_F}{k_B T}\right)} \qquad \textbf{(3)}$$

Where E_F is the Fermi Energy and k_B is the Boltzmann constant. The Fermi Energy carries information on the average energy of electrons in a material, effectively describes the relative charge carrier density, and represents the systems majority charge carrier.

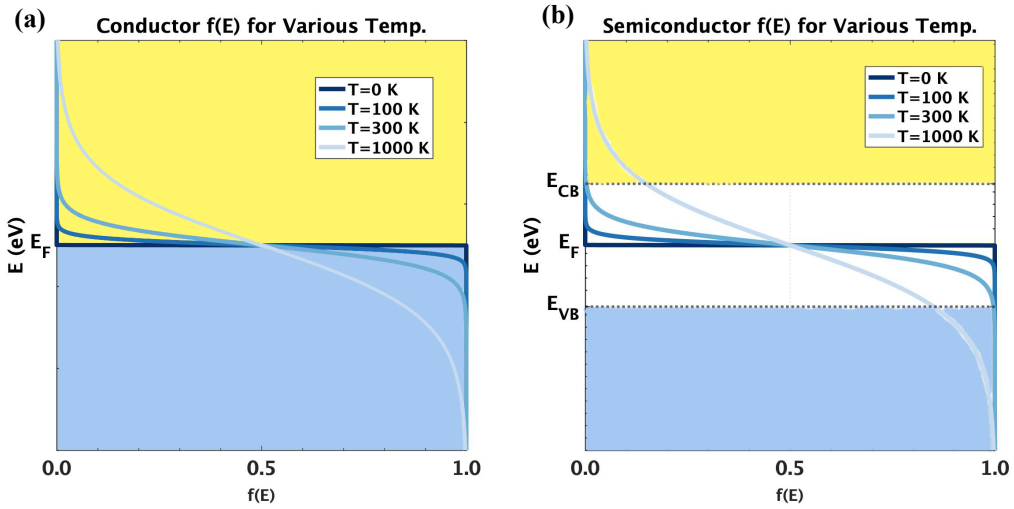

Figure 2.5: The Fermi-Dirac distribution function at various temperatures for a **(a)** conductor and **(b)** semiconductor.

An illustration of $f(E)$ and the impact temperature has on electron occupation can be seen above in Figure 2.5. At 0 °K, all the allowed energy states below E_F are occupied and above E_F unoccupied. At T > 0 °K, electrons gain enough thermal energy to exist in some states above E_F. In semiconductors there are no allowed states in the bandgap and thermalized electrons above E_F exist in the VB, while all other electrons below E_F exist in the CB. The total concentration of electrons in the CB and holes in the VB can then be obtained through multiplying $g(E)*f(E)$ and integrating across the energy band.

$$n = \int_{E_{CB}}^{E_{top}} g_c(E) * f(E)dE = N_C * exp\left(\frac{E_F - E_{CB}}{k_B T}\right) \quad \textbf{(4)}$$

$$p = \int_{E_{bottom}}^{E_{VB}} g_v(E) * f(E)dE = N_V * exp\left(\frac{E_{VB} - E_F}{k_B T}\right) \quad \textbf{(5)}$$

Where N_C and N_V are the effective densities of the CB and VB energy states, respectively.[1,9]

2.2.4 Intrinsic and Extrinsic Semiconductors

In an intrinsic, *i*-type, semiconductor there exists an equal number of charge carriers, $n=p$. We can calculate E_F for an intrinsic semiconductor at T = 0 °K by combing the equations (4) and (5) to get equation (6) below.

$$E_F = \frac{E_{CB}+E_{VB}}{2} + \frac{k_B T}{2} ln\left(\frac{N_V}{N_C}\right) \qquad \textbf{(6)}$$

It becomes mathematically clear that at absolute zero, 0°K, the Fermi energy falls directly in the middle of the bandgap. Since $\frac{N_V}{N_C} \sim \frac{m_p^*}{m_n^*}$, and typically $m_p^* > m_n^*$, E_F tends to increase for elevated temperatures. In extrinsic semiconductors, the carrier concentration has been modified such that $n \neq p$. This can be done intentionally, like doping in silicon, or arise naturally due to point defects in a crystal's structure. Extrinsic semiconductors are characterized as either *n*-type or *p*-type depending on the majority charge carrier.[1,9]

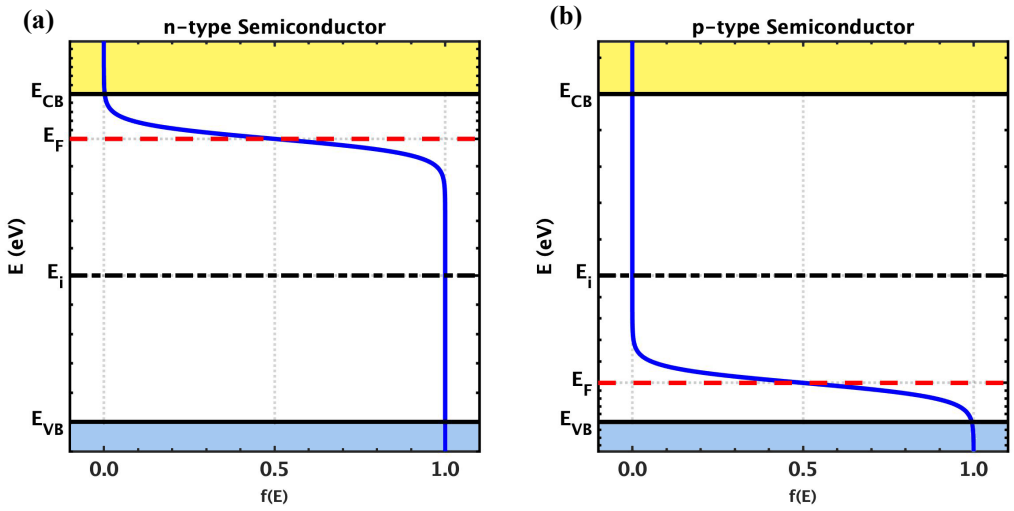

Figure 2.6: Relative Fermi Energy level for **(a)** *n*-type and **(b)** *p*-type semiconductors.

Extrinsic semiconductors are most commonly made through intentional doping. *n*-type Si is fabricated by inserting donor atoms into Si's crystal structure. Donor atoms, like phosphorous

(P), contain five valence electrons compared to Si's four. When the P atom fills a spot in the Si lattice, the fifth electron does not contribute to bonding and becomes weakly bound. At room-temperature the P atoms become ionized and the electrons liberated. These electrons are localized in the vicinity of the donor atoms and have energy close to CB but do not truly lie in the CB. Therefore, the insertion introduces allowed energy states in the forbidden bandgap region position extremely close to the CB and raising the Fermi energy. In similar fashion, introducing acceptor atoms with three valence electrons, like boron (B), increases the hole concentration to make *p*-type Si. The addition of acceptor ions overall lowers the Fermi energy. Although impurity addition is the most well know technique to intentionally dope semiconductors, it is certainly not the only method. CdTe semiconductors are doped through nonstoichiometric addition of one element during synthesis. In metal oxides doping can take effect naturally through point defects and oxygen vacancies.[1,8,9,10]

2.3 Basic Photovoltaic Performance Metrics

A solar cell is an optoelectronic device that absorbs light and converts it directly into electricity. The absorbed light energy creates current and voltage, thus generating power. This physical phenomenon is called the photovoltaic effect and is basis on which all solar cells operate. First and foremost, this process requires a material that can absorb light energy to promote electrons to higher energy states. After electron-hole pairs are generated they must flow in opposite directions where they can be collected in an electrical circuit. The process can ultimately be broken down into three main events: generation of charge carriers due to absorption, separation of the photo-generated charge carriers, and lastly collection of charge carriers.

2.3.1 *Current-Voltage (JV) Measurement*

Most of the important metrics of solar cell performance can be extracted by measuring current-voltage (JV) response under illumination. This can be done simply by illuminating the cell with a simulated solar spectrum, applying a bias directly across the device, and measuring the resulting current flow. Analysis of the curve allows for the extraction of certain metrics which can give an insight into the solar cells ability to produce electricity efficiently.[1,11]

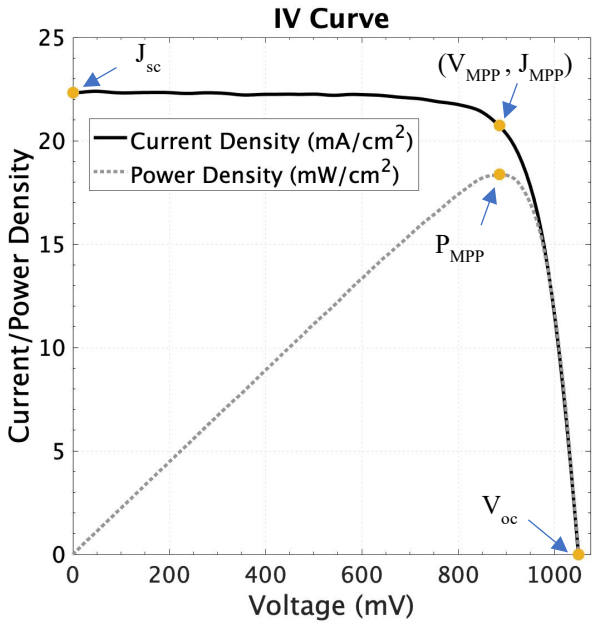

Figure 2.7: Typical JV curve highlighting a few important performance characteristics.

2.4.2 *Reference Solar Spectrum (AM1.5)*

The sun emits a radiation spectrum similar to the of a blackbody at 6000 °K. AM0 represents the raw solar spectrum incident on the atmosphere's surface. As light passes through the atmosphere is attenuated due to scattering and absorption from ozone and other air molecules. The actual amount of radiation that reaches earth's surface is dependent on a wide variety of conditions such as the sun's location in the sky and local atmospheric conditions. In order to

standardize PV testing, the AM1.5 spectrum was adopted as the industrial reference solar spectrum. It corresponds to an irradiance of 1000 $W \cdot m^{-2}$ and is close to the maximum value that earth receives on average.[1,11,12]

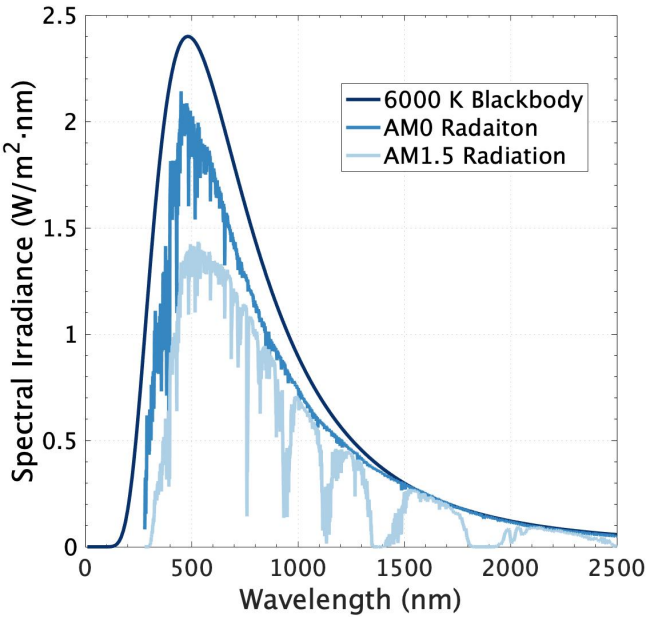

Figure 2.8: Terrestrial AM1.5 and extraterrestrial AM0 solar spectrum compared to a blackbody spectrum of a blackbody at 6000 °K.

2.4.3 Short Circuit Current (J_{sc})

The short circuit current is the maximum current that can be extracted from a solar cell. It occurs at zero applied bias; resulting from the generation and collection of light-generated carriers. A solar cell's J_{sc} depends on a number of parameters, but a few important ones are listed below: [1,11]

- Solar cell area; however, this dependence is commonly removed by dividing the J_{sc} by the active area to get a current density in mA/cm^2

- Light intensity; current is a function of carriers generated from photon absorption. Increasing the number of photons increases the amount generated charge carriers, and therefore increasing the current
- Optical properties such as absorption, reflection, and transmission.

2.4.4 Open Circuit Voltage (V_{oc})

The open circuit voltage V_{oc} is the maximum possible voltage a device can deliver. At V_{oc}, the applied bias cancels out the solar cell's built-in potential and removing the driving force for generated charges to be collected. Therefore, at V_{oc} there will be no current flowing through the devices external circuit.[1,11]

2.4.5 Fill Factor (FF)

Although the J_{sc} and V_{oc} relate to the maximum current and voltage that a solar device can deliver, at these points there no power is generated. The FF is the parameter that ties these two values together to determine the maximum power the solar cell can produce. FF is the ratio of the solar cell's MPP to the product of V_{oc} with J_{sc} and relates to the solar cell's deviation from ideal behavior. Graphically, it is the area ratio of the largest rectangle formed than can be formed within the JV curve to the area rectangle created by multiplying V_{oc} with J_{sc}.[1,11]

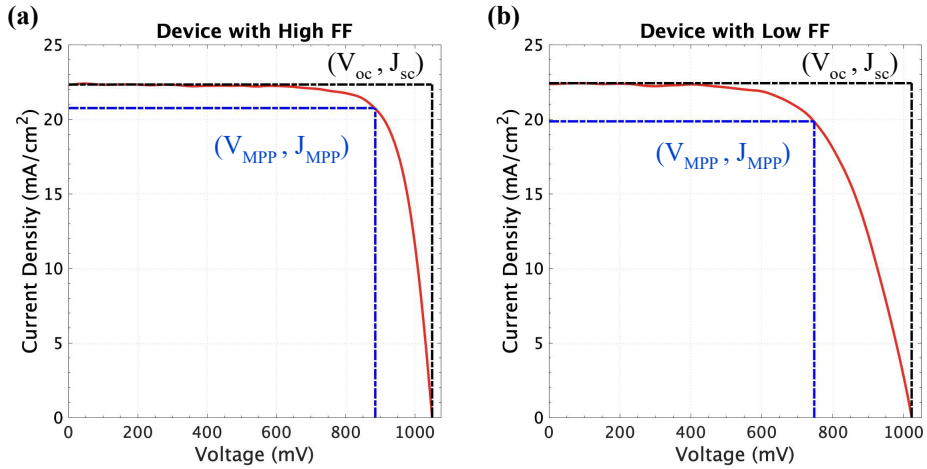

Figure 2.9: Illustration of a JV curve with **(a)** high FF and **(b)** low FF.

$$FF = \frac{V_{MPP}J_{MPP}}{V_{oc}\,J_{sc}} \qquad \textbf{(7)}$$

2.4.6 Power Conversion Efficiency (PCE)

The PCE ultimately combines the individual parameters into one value that can be used to cross compare solar cell performance. It is the ratio of energy output to energy input from the sun and is the most commonly used metric a to characterize a solar cell's ability to convert light into electricity.

$$PCE = \frac{P_{max}}{P_{in}} = \frac{V_{oc}\,J_{sc}FF}{P_{in}} \qquad \textbf{(8)}$$

Where for standard testing P_{in} corresponds to the AM1.5 spectrum irradiance value of 1000 $W{\cdot}m^{-2}$.[1,11]

2.4.7 Parasitic Resistive Effects: Series (R_s) and Shunt (R_{SH}) Resistance

Parasitic resistive effects in solar cells can have large impacts on performance and greatly reduce efficiencies. The most commonly encountered resistances in solar cells are series, R_s, and shunt, R_{SH}, resistance, both of which can be detrimental to a solar cell. Large R_s results in power

loss by resisting the flow of electrons and hindering the ability to extract current. Power losses due to R_S mainly arise from energetic barriers or bulk resistances within materials. Sources of R_S are typically interfaces, sheet resistances and, bulky layers. R_{SH} results when there are alternate pathways for generated current to flow in a solar cell. When R_{SH} is low, light-generated current flows into undesirable regions, resulting in current and power losses. R_{SH} usually results from manufacturing defects rather than the material properties. The type of resistance being encountered can be identified by based on the regions where the JV curve deviates from ideality,

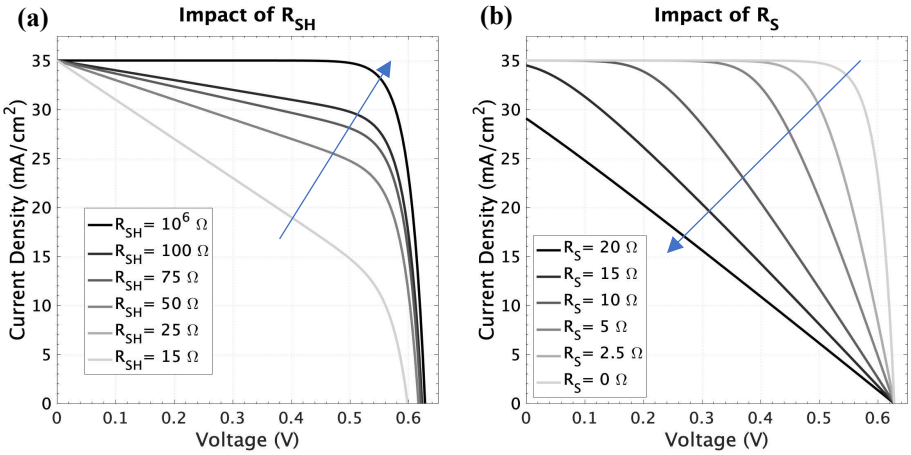

Figure 2.10: Illustration of the effects **(a)** R_S and **(b)** R_{SH} have on a JV curve.

High performing solar cells rely on minimizing R_S and maximizing R_{SH} to mitigate current or voltage drops. Effects from low R_{SH} and high R_S are displayed in Figure 2.10.[1,11]

Chapter 3

SnO_2 for Perovskite Solar Cell Application

3.1 Perovskite Solar Cells (PSCs)

Fundamentally, PSCs operate based on the three physical principles any solar cell rely on and utilize five composite layers to do. In the middle, a perovskite absorber is sandwiched between a hole transport layer (HTL), an electron transport layer (ETL), with contacts on both sides. The front contact is a typically a (transparent conducting oxide) TCO, like FTO or ITO, sputtered on glass and the back contact is usually a thermally evaporated metal like gold. The overall structure is classified as either regular (n-i-p) or inverted (p-i-n) depending on the charge transport layers' (CTLs) orientation, with respect to incident light. The structure can then be further classified as planar or mesoporous depending on the ETL structure. The planar structure consists of an essentially flat ETL-perovskite, while for mesoporous devices the perovskite infiltrates into the ETL using it as scaffold.[13,14,15] Figure 3.2 illustrates the differences structures for each of the classifications described.

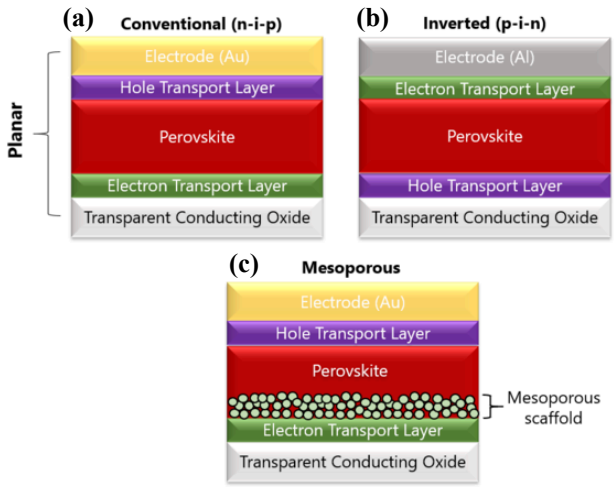

Figure 3.1: Commonly employed **(a)** regular, **(b)** inverted, and **(c)** mesoporous (regular) PSC device structures.[14]

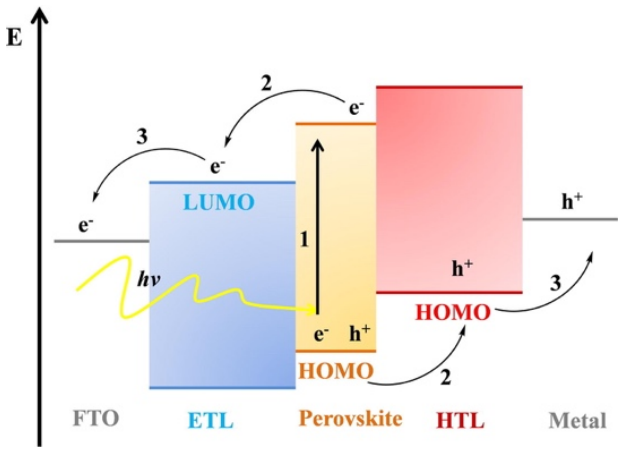

Figure 3.2: Operation and electronic band alignment of a PSC.[16]

Charge selective layers play an essential role in extracting current from PSCs by ensuring that current only flows in one direction. Some efforts have been made to remove CTLs from devices, but their operation, specifically J_{sc}, is severely reduced. Figure 2.4 illustrates the band alignment PSCs operate based on, in accordance with the three main operating principles. In step one, incident photons excite charge carriers to their respective energy bands. The charge carriers are separated based on specific electronic alignments of the materials' energy bands. At the ETL interface, the CBM offset is energetically favorable such that electrons, but not holes, will move across the barrier. Conversely, at the HTL interface, the VBM alignments facilitates holes, but not electrons, across the boundary.[14,15,16]

3.2 SnO_2 as Electron Transport Layer

All ETLs are wide bandgap n-type semiconductors and a variety of materials have been employed to produce high efficiency PSCs. Unfortunately, many of them lack the chemical or photo stability required for long-term application. The first PSC design was based on a dye-sensitized solar cell (DSSC) and as a result, the most commonly employed ETL to date has

been TiO_2.[17] TiO_2 maintains a good band alignment with the perovskite, is reasonably conductive, and has been used to produce the highest PCEs to date. The alternative downside is that TiO_2 exhibits strong UV spectral absorption and only crystallizes at high temperatures, >500 °C. The combined photoactivity, creating photocatalytic degradation mechanisms, and high-temperature processing, limiting available substrates, has called into question TiO_2's wider and long-term use as an ETL for PSCs. A variety of other n-type inorganic materials such as ZnO, Zn_2SO_4, CdS, and $BaSnO_3$ have been explored as replacements to TiO_2. Although these materials initially appeared advantages over TiO_2, they were shown to have their own disadvantages related to either chemical, thermal, or UV instability. Various organic polymer ETLs have also yielded high efficiency PSCs, but their expensive nature negates the cost advantage of perovskite and thermal instability degrades devices quickly.[18,19]

Among the TCOs explored, SnO_2 has emerged as the superior ETL material. SnO_2 has excellent CB alignment, a deep VB, high electron mobility, low UV-Vis optical absorption, and excellent chemical stability. In addition, fluorine doped SnO_2 (FTO) is one of the best front contact TCO materials for solar cell application. SnO_2 has a wide range of E_g's reported in literature ranging from ~3.5 eV to 4.0 eV, with some reporting values as high as 4.4 eV for amorphous SnO_2. SnO_2's CB energy lies at about 4.5 eV (abs. vs vacuum), which is suitably lower than reported photovoltaic perovskite materials that typically exist around 3.4-3.9 eV. SnO_2's CB is primarily derived from Sn 5s and O 2p orbital interaction, giving rise to a high CB dispersion. The large dispersion is the reason for a low charge effective mass and high electron mobility. Higher electron mobility, compared to that of TiO_2, increases the efficiency of extraction at the SnO_2-perovskite interface and theoretically increases all PV performance

characteristics like J_{sc}, FF, R_s, and R_{sh}. SnO_2 also yields high performance at low-temperature processing, lowering manufacturing costs and opening possible development on flexible substrates. Furthermore, PSCs' notably suffer from high instability in atmosphere and at contact interfaces, but SnO_2's high chemical stability and low hygroscopicity can effectively increase PSC stability for larger and longer real-world applications.[19,20,21,22]

3.3 Common Methods of SnO_2 ETL Deposition

A variety of techniques have been utilized to fabricate SnO_2 thin films for ETL purposes, but the following methods discussed are the most commonly reported throughout literature.

3.3.1 Spin Coating (SC)

Spin-coating is by no surprise the most commonly reported SnO_2 deposition technique. Most reports achieve synthesis through depositing an SnO_2 colloidal or nanocolloidal precursor solution on the rotating substrate, followed by a subsequent annealing in ambient conditions. Both precursors are typically composed of $SnCl_2$, $SnCl_4$, or their hydrate counterparts ($SnCl_2 \bullet 2H_2O$ and $SnCl_4 \bullet 5H_2O$) dissolved in anhydrous ethanol. The nanocolloidal solution receives an additional surfactant, like TMAH, and then undergoes thermal treatment. The nanoparticles are then dispersed in isopropyl and deposited. Both precursors are deposited the same way, with the main difference being SnO_2 particle size. Both approaches have produced high-efficiency PSCs, but spin-coating has many shortcomings and is unsuitable for industrial purposes. Some difficulties with spin-casting are its low material utilization, difficultly to scale over large substrates, high film uniformity, and poor reproducibility.[19,24]

3.3.2 Chemical Bath Deposition (CBD)

CBD is a well-studied solution-growth technique that has been established for CdS and ZnO thin film deposition in CIGS solar cells. Its inexpensive, easy to perform, and well-suited for large area deposition. CBD involves basically two steps, nucleation followed by particle growth. Thin film growth can be tuned through modifying conditions such as bath temperature, pH, reaction time, and reactant concentrations. CBD has potential for commercial SnO_2 application, but it does have some notable disadvantageous. Although simple to perform and fairly reproducible, each deposition produces large volumes of waste. The films generated can also contain elevated impurity concentrations due to the technique's chemical nature. Furthermore, reaction conditions need be optimized for distinct substrates to guarantee proper growth and coverage.[18,19]

3.3.3 Atomic Layer Deposition (ALD)

ALD technology offers the finest control over thin film thickness and is an exceptional technique for ETL fabrication. It is a subclass of CVD performed by periodically exposing substrates to precursors, generating self-limiting reactions at the substrate surface to form monolayers of material. It can produce highly compact ETLs, at low temperatures, and has also been utilized to fabricate high efficiency devices. The main benefits of employing ALD synthesis are its exceptional thickness control, ultra-conformal growth, and highly compact layer formation. Unfortunately, current ALD techniques are expensive, time consuming and not a viable for mass production.[19]

Chapter 4

Experimental

4.1 Photovoltaic Device Fabrication

4.1.1 Substrate Preparation[26]

TEC15 FTO (~13 Ohm/sqr) substrates were partially covered with zinc powder and chemically etched by dropping 2 M HCl continuously until bubbling stopped. The substrates were then cleaned through a series of sonication baths. The procedure is as followed:

- 10 min. ultrasonic bath in 2% by volume Hellmanex glass cleaning solution in DI water.
- 10 min. ultrasonic bath in isopropanol solution.
- 10 min. sonication in 200 proof ethanol solution.
- Substrates were then blow dried and plasma cleaned for 10 min. on maximum power prior to SnO_2 deposition.

4.1.2 Electron Selective Contacts

4.1.2.1 SnO_2 by Vacuum Thermal Evaporation (vte)

Prior the ETL deposition, a small region of FTO opposite the etched region was masked for later contact. Pure SnO_2 nanopowder was then deposited via thermal evaporation in an ultrahigh vacuum. The SnO_2 powder was evaporated from an alumina coated tungsten boat at pressure below < $1x10^{-6}$ mbar. Deposition rates and thicknesses were monitored in-situ with a QCM. Final thin film thicknesses varied, and the rate of evaporation was typically fixed at ~0.25Å/s (1.5 nm/min). The substrates were rotated throughout deposition to ensure film

uniformity and reduce shadowing effects. Post deposition, the films were removed from the glovebox and annealed in a box furnace at 180 °C for 1hr.

4.1.2.2 SnO_2 by Spin Coating and Chemical Bath Feposition (sccbd)[18]

A 0.1 M solution of $SnCl_2$ in dry ethanol was deposited on the FTO substrates by spin coating at 3000 rpm for 20s followed by an annealing 180 °C for 1hr. The samples were then placed in a CBD bath containing 80.0 mL DI water, 1.0 µL mercaptoacetic acid (thioglycolic), 50.0 µL of 37% HCl, 10.0 mg $SnCl_2 \cdot H_2O$, and 50.0 mg urea at 75 °C for 1h. Samples were then removed from the bath, air dried, and annealed in a box furnace at 180 °C for 1hr.

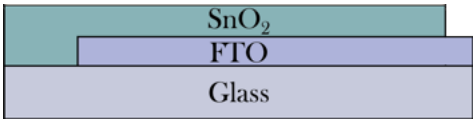

Figure 4.1: Cross section of architecture after etching and SnO_2 ETL deposition.

4.1.3 $Cs_5(FA_{0.83}MA_{0.17})_{95}Pb(I_{0.83}Br_{0.17})_3$ Triple Cation Perovskite Absorber[26]

A Cs-doped triple cation perovskite absorber, $[Cs_5(FA_{0.83}MA_{0.17})_{95}Pb(I_{0.83}Br_{0.17})_3]$, layer was deposited on the SnO_2 ETLs via a two-step anti-solvent drop procedure. $FAPbI_3$ has an admirable E_g, but its photoactive black phase is thermodynamically unstable below 150 °C. $MAPbX_3$ addition is known to improve $FAPbI_3$ structurally and chemical stability below 150 °C, so $MAPbBr_3$ to improve device performance. Moreover, additional inorganic CsI was also added to further increase the long-term stability in ambient conditions. Individual 1.5 M precursors of PbI_2 and $PbBr_2$ were initially prepared by dissolving the respective salts in a mixed solvent of 4:1 (V/V ratio) DMF:DMSO. Precursor densities were then measured to back out the true molarity of the respective solutions. FAI and MABr powders were then weighed out in separate vials and the respective lead halide precursors were then added to make solutions with 9% Pb excess (1:1.09 molar ratio of FAI:PbI_2 and MABr:$PbBr_2$). The $FAPbI_3$ and $MAPbBr_3$ solutions

were then mixed in a separate vial in a 5:1 V/V ratio $FAPbI_3$:$MAPbBr_3$. Cs doping was then performed by adding 5% vol 1.5 M CsI stock solution to the overall mixed FAMA solution. After fully mixing, the final triple cation perovskite solution has been prepared and ideally has a nominal stoichiometry of $[Cs_5(FA_{0.83}MA_{0.17})_{95}Pb(I_{0.83}Br_{0.17})_3]$. SnO_2 ETLs were plasma treated at maximum power for 10 min prior to perovskite deposition. The perovskite solution was then spin coated on the FTO/SnO_2 substrates via a two-step procedure anti-solvent drop procedure. (1000rpm for 10s and 6000rpm for 20s). 200 µL of chlorobenzene (CB) antisolvent was dropped on the film center with 5s of spinning left in the second step. The films where then annealed 100 °C for 50min.

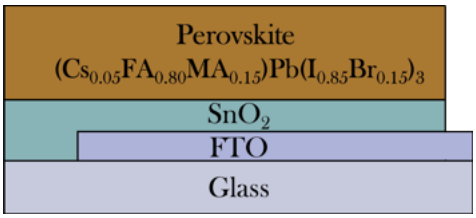

Figure 4.2: Cross section of architecture after etching, SnO_2 ETL deposition, and perovskite deposition.

4.1.4 Hole Selective Contact and Metal Electrode Deposition[26]

A 65 mM solution of spiro-OMeTAD in CB was prepared and doped with 4-*tert*-butylpyridine (TBP) and bis(trifluoromethylsulfonyl)imide lithium salt (Li-TFSI) at molar ratios of 3.3 and 0.5, respectively. The solution was then spin coated in a single step of 4000rpm for 20s, dropping 70 µL of solution in the middle of the film with 15s left of spinning. The samples were then stored overnight in dry, dark air to allow the lithium doping to take effect. A 50 nm thick gold top contact was then thermal evaporated by under vacuum at a constant rate of 0.3 - 0.4 Å/s.

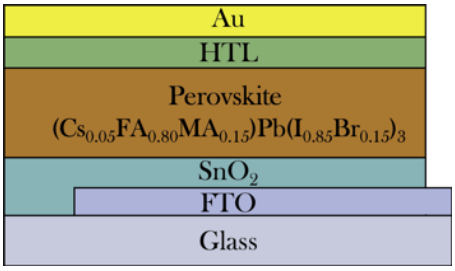

Figure 4.3: Finished PSC device architecture.

4.2 Characterization

4.2.1 Ultraviolet–Visible (UV-Vis) Spectrophotometry

Transmission measurements were obtained with a Perkin Elmer Lambda 950 UV-Vis-NIR spectrophotometer, integrating sphere module. The light was sourced from deuterium (250-320nm) and tungsten (320-860) lamps. Light intensities were measured by a photomultiplier tube (PMT) with a spectral resolution of 0.1 nm. After transmission measurements were taken, the resulting data was converted to a Tauc plot for optical E_g analysis. By extrapolating the absorption onset to the x-axis, material bandgaps can be determined.[27]

$$(\alpha h\nu)^{1/r} = A\left(h\nu - E_g\right) \qquad \textbf{(9)}$$

$$h\nu = \frac{1240\ (eV \cdot nm)}{\lambda(nm)} \qquad \textbf{(10)}$$

Where α is the absorption coefficient, $h\nu$ is the wavelength energy, A is a proportionality factor, and r a is a number determined by the nature of the optoelectronic transition. For direct allowed transitions, like in SnO_2, $r = \frac{1}{2}$. The % transmittance can be converted to absorbance, which is proportional to the absorption coefficient and used in place of the α in equation 9 with equation 11 below.[27]

$$\alpha \approx Abs = \log_{10}\left(\frac{I_o}{I}\right) = 2 - \log_{10}(\%T) \qquad \textbf{(11)}$$

4.2.2 Cyclic Voltammetry (CV)

CV measurements were performed with an EC-Lab Biologic in a 3-electrode configuration. A Pt-wire served as the counter electrode and an Ag/AgCl (KCl sat'd) as the reference electrode. The electrolyte solution was 1.0 mM $K_4Fe(CN)_6$ + $K_3Fe(CN)_6$ in aqueous 0.5 M KCl solution, pH = 7. Measurements were conducted at low scan rate, 20 mV/s, to reduce the effects of solution series resistance. Four cycles were recorded wherein the third cycle typically showing a stabilized scan. The working electrode, samples, was contacted via alligator clip and sealed with Kapton tape, which determined the active surface area exposed to electrolyte. CV measurements were conducted to verify ETL coverage over the FTO surface and CB energy levels. Redox reactions can be used to determine the effective coverage of a material on a conductive substrate. In order to do so, the redox-potential must be sufficiency positive to the CB of the material of interest. If the substrate is fully covered, the redox reaction will be completely suppressed, and no current will be recorded. However, incomplete surface coverage, caused by cracks or pinholes, will result in electrical current. CB energy level information can be gained through cathodic onset potentials. Theoretically, if the surface is fully covered, then sharp increase in current should be seen when the applied bias raises the energy of the electrode's electrons up to the CB energy.[18,28,29]

4.2.3 Potentiostatic Electrochemical Impedance Spectroscopy (PEIS)

PEIS measurements were performed prior to CV measurements for ohmic drop determination. The ohmic drop is the series resistance in solution between the working and reference electrode. The ohmic drop can vary for a variety of reasons and performing this step reduces the day-to-day experimental variation. PEIS was performed three times at V_{oc} vs the

working electrode, scanning frequency from 200 kHz to 100 mHz, with a sinus amplitude of 15.0 mV. The solution resistance was then compensated at 85% during CV measurements.[29]

4.2.4 Ellipsometry

Ellipsometry measurements are performed by measuring the polarization change of light after reflection from or transmission through a sample. The change in polarization depends on the material's complex dielectric function and index dispersion. Ellipsometry can be used to measure thin film thicknesses of transparent or lightly absorbing films on optically smooth reflective substrates.[30] vte-SnO_2 thickness measurements were performed with a J.A. Woollam M-2000D Ellipsometer. Films were deposited on polished silicon wafers and take to Nano3 for characterization. Data acquisition and model fitting was done with CompleteEASE software to generate thickness and mean square error results.

4.2.5 Scanning Electron Microscopy (SEM)

SEM images were taken on a Zeiss Sigma 500 SEM in Nano3 and EDX on the FEI Apreo FESEM in the Structural and Material Engineering building basement.

4.2.6 Steady-state Photoluminescence (PL) Mapping

Photoluminescence mapping measurements were performed with a Renishaw inVia Qontor Confocal Raman Microscope. All measurements were done with a 633nm laser line, a 1200 grating at magnification objectives of either 50x, 20x, or 5x.

4.2.7 Current-Voltage (JV) Characteristics

PSC photovoltaic performance was measured under an AM1.5 simulated spectrum from a Newport 1600 W Arc Lamp Power Supply at 1000 $W \cdot m^{-2}$ calibrated by a certified reference silicon solar cell. The Au and FTO sections were contacted via spring loaded metal pogo-pins to ensure non-damaging device contact. The defined active area tested on each device varied from 0.04 cm^2 – 0.08 cm^2, determined by a black sheet aperture mask. A Kepco BOP 100-4D sourced voltage, while two Keysight 34465A multimeters measured current in a 4-wire setup. The voltage sweep range was determined automatically by the Tracer software based on an initial V_{oc} measurement. The voltage was then swept in steps 0.01 V and a scan rate of 0.2 V/s. The IV curve parameters such as Voc, Jsc, FF, and PCE were all displayed immediately with the Tracer software analysis.

4.2.8 External (EQE) and Internal (IQE) Quantum Efficiency

EQE measures the portion of incident photons that are converted to collected carriers at each wavelength. From the EQE, the Jsc can be calculated through integration with the AM1.5 spectrum.[1]

$$J_{sc} = -e \int_{-\lambda}^{\lambda} EQE(\lambda) * \phi_{AM1.5}(\lambda)\, d\lambda \qquad \textbf{(12)}$$

Where e is the elementary charge and $\phi_{AM1.5}(\lambda)$ is the incident photon flux based on the AM1.5 spectrum. The IQE is measures the portion of light that reaches the absorber and gets converted to collected charge carriers. It is calculated by dividing the EQE by the percent of non-reflected light, usually determined through UV-Vis spectrophotometry.[1]

$$IQE = \frac{EQE}{(1-R(\lambda))} \qquad \textbf{(13)}$$

Where $R(\lambda)$ is the percent of reflected light per wavelength. EQE measurement were performed over wavelengths from 250 – 850 nm with a 10nm step size. Calibration was performed prior to data collection with a silicon photodiode, aperture to the same hole size in corresponding IV measurements. Light generated by a Xe arc lamp powered Newport OPS-A500 arc supply was sent through a Newport CS260 UV-Vis monochromator to select desired wavelengths. A Thor Labs MC2000B optical chopper system and Stanford Research systems Lock-In Amplifier were then used to amplify and measure the resulting current signal at each wavelength.

Chapter 5

Vacuum Thermal Evaporated SnO_2 ETL

5.1 Introduction

Over recent years the research community has experienced a surge in reports focused on fabricating large-area PSC modules in the hopes of moving towards a commercial product. In order for PSCs to produce energy cost savings and reach their full potential, it is necessary to demonstrate their compatibility with industrial manufacturing techniques. Recent progress in scaling the perovskite absorber has displayed promising results, however, the modules presented in almost all large-area works are assembled with ETLs impractical to commercialization. To date, the large-area PSC community has systematically researched scalability with insufficient reports on transport layer commercialization, specifically SnO_2 ETL industrial manufacturability. SnO_2 is a low-cost ETL material that has shown to produce high-efficiency, stable PSCs. Therefore, it is desirable to advance commercially compatible SnO_2 manufacturing techniques.[23,24,25] Herein, vacuum thermal evaporation is employed to fabricate high-quality SnO_2 (vte-SnO_2) ETLs, superseding our sccbd-SnO_2 baseline ETL. The advantages of utilizing vte-SnO_2 ETLs in PSC devices are higher V_{oc}, better reproducibility, excellent thicknesses control, and almost 100% reduced waste production. This approach constitutes a simple, scalable, and easily automated deposition method paving way towards the industrialization of PSCs. Lastly, the vte-SnO_2 deposited over a 100 cm^2 FTO substrate and individual sections are characterized to illustrate negligible variation across the larger surface.

5.2 Vacuum Thermal Evaporation

Vacuum thermal evaporation is a commonly employed physical vapor deposition (PVD) technique. Fundamentally, PVD techniques have three main steps. First material is vaporized from a pure source. The vapors are then travel through a vacuum to the substrate surface. Then as the vapors reach the substrate surface, they condense to form a thin film. Vacuum conditions are essential to ensure material vapors can travel freely to the substrate and will not be impacted by air molecules in the chamber. There are a variety of PVD techniques that exist, distinguished by how they achieve the first step of material vaporization. In thermal evaporation, material is vaporized by resistively heating the material on a refractory metal like tungsten (W). Benefits of thermal evaporation are its ease to perform, excellent material utilization, high purity, reproducibility, and small amount of substrate heating. When depositing thin films for PV application, complete surface coverage and film thickness uniformity are very important. The excellent coverage achieved is displayed experimentally in the results section. Confidence in the thickness uniformity across large-areas is established with calculations below. Studies have shown that devices fabricated with different ETL thicknesses, yield different performances. Performance variation resulting from different ETL thickness results from tradeoffs between R_S and R_{SH}, and usually requires repeated fabrication steps to be optimized. Thickness optimization is easily performed with vte since one can fabricate films with a variety of thicknesses quickly and accurately. However, the purpose of this section is to support the statement that vte can confidently deposit uniform films over a 100 cm^2 FTO region sufficiently.

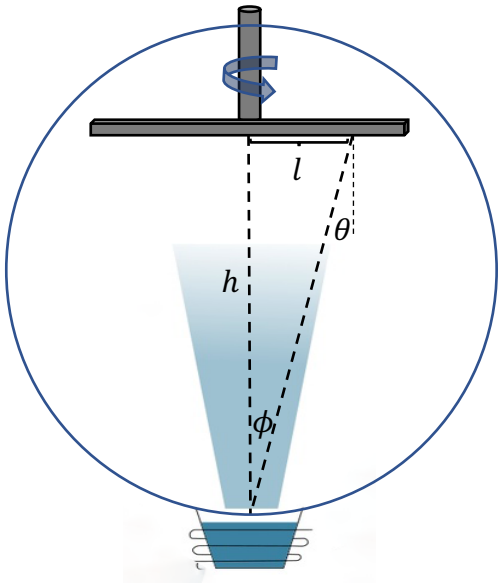

Figure 5.1: Depiction of thermal evaporation setup and angular decencies.

Rates of evaporation and subsequent deposition have angular dependencies described by a cosine law. A fundamental analysis starts with treating the evaporation source as an infinitely small point source and builds up from there. Fortunately, evaporation techniques are well studied, the equations describing this process have been derived, and are easily located in evaporative technique textbooks. Therefore, the thickness variation across a planar substrate with material evaporating from a surface source can be described by the equation below.[31]

$$\frac{d}{d_0} = \frac{1}{\left(1+\left(\frac{l}{h}\right)^2\right)^2} \qquad \textbf{(14)}$$

Where d_0 is the thickness at the center of the substrate, d is the thickness at any point, l is the distance from the center, and h is the distance from the source to the substrate. Equation 14 has been normalized to remove any angular dependence, making the solution easy to calculate. Although equation 14 does not account for substrate rotation, the effect only aids to increase surface uniformity. Utilizing equation 14, Figure 5.2 displays the calculated thickness variations that would be observed across a 100 cm^2 and a 2500 cm^2 substrate in the Fenning research lab's

thermal evaporator. The largest variation we expect to occur at the corners, and across the 100 cm^2 surface the difference doesn't exceed 2 Å. Even as we scale to 25x the area, only a 4 nm drop is observed. In addition, there are ways to even further mitigate any thickness variations for optoelectronics where thickness uniformity is essential to high performance.

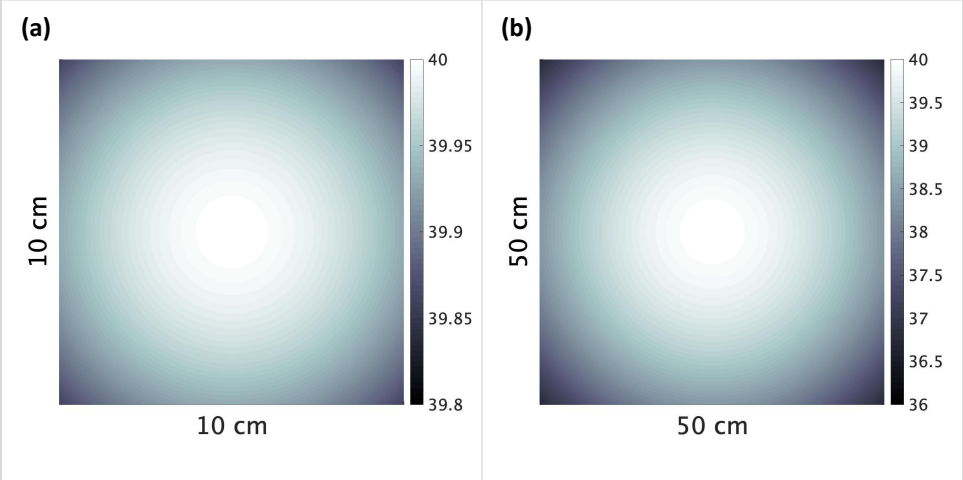

Figure 5.2: Calculated substrate thickness variations across a **(a)** 100 cm^2 and **(b)** 2500 cm^2 substrates for h = 120 cm and d_0 = 40 nm.

5.3 Results and Discussion

5.3.1 SnO_2 ETL Characterization

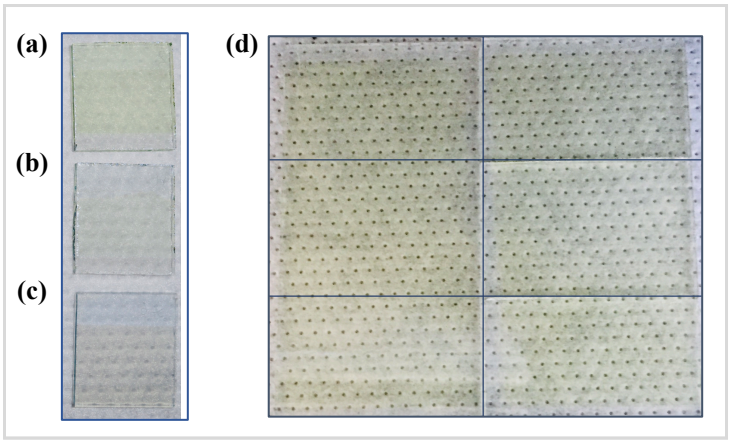

Figure 5.3: Pictures of substrates containing **(a)** as-deposited vte-SnO_2 **(b)** annealed vte-SnO_2 **(c)** sccbd-SnO_2 and **(d)** annealed vte-SnO_2 on a 100 cm^2 substrate.

The initial scope of this work was centered around developing an as-deposited MO charge transport layer. This development would enable the ability to deposit directly atop the perovskite absorber with no additional processing and would be quite revolutionary. Unfortunately, the as-deposited vte-SnO_2 proved unable to efficiently extract electrons when placed in a perovskite solar cell. Looking at images of as-deposited, Figure 5.3a, and annealed, Figure 5.3b, vte-SnO_2, shows that before annealing the SnO_2 films contain a slightly yellow hue. Post-annealing the vte-SnO_2 films more closely resemble the sccbd-SnO_2 baseline. This basic observation combined with a brief literature search lead to a prediction that the as-deposited SnO_2 films are most likely under-stoichiometric, containing variable valence Sn states, like Sn^{2+}. Sn^{2+} doped SnO_2 (Sn^{2+}-SnO_2) composites have been synthesized for photocatalytic purposes and have been shown to be yellow due to increased absorption in the visible spectrum.[32] Fortunately, Sn^{2+} is easily oxidized to Sn^{4+} at elevated temperatures in air and with a brief low-temperature anneal the evaporated thin films were converted to a suitable ETL. Furthermore, this effect can also be seen with Figure 5.4a, wherein the as-deposited vte-SnO_2 films have slightly increased absorption in the visible spectrum over wavelengths from ~550-300nm. Moreover, the as-deposited films display a lower E_g, which is representative of Sn^{2+} states existing in the film. Both SnO and Sn^{2+}- SnO_2 are reported to have lower E_g values than SnO_2.[24,25,32] After annealing, the vte-SnO_2 samples have transmission and E_g values that more closely resemble the sccbd-SnO_2 baseline. Moving to the right side of Figure 5.4, the same analysis is performed for sections of the large-area deposited vte-SnO_2 surface. Small value fluctuations should be apparent in the Tauc plot, after squaring the log(%T), and there is essentially no variation in either the transmission of E_g across the 100 cm^2 region.

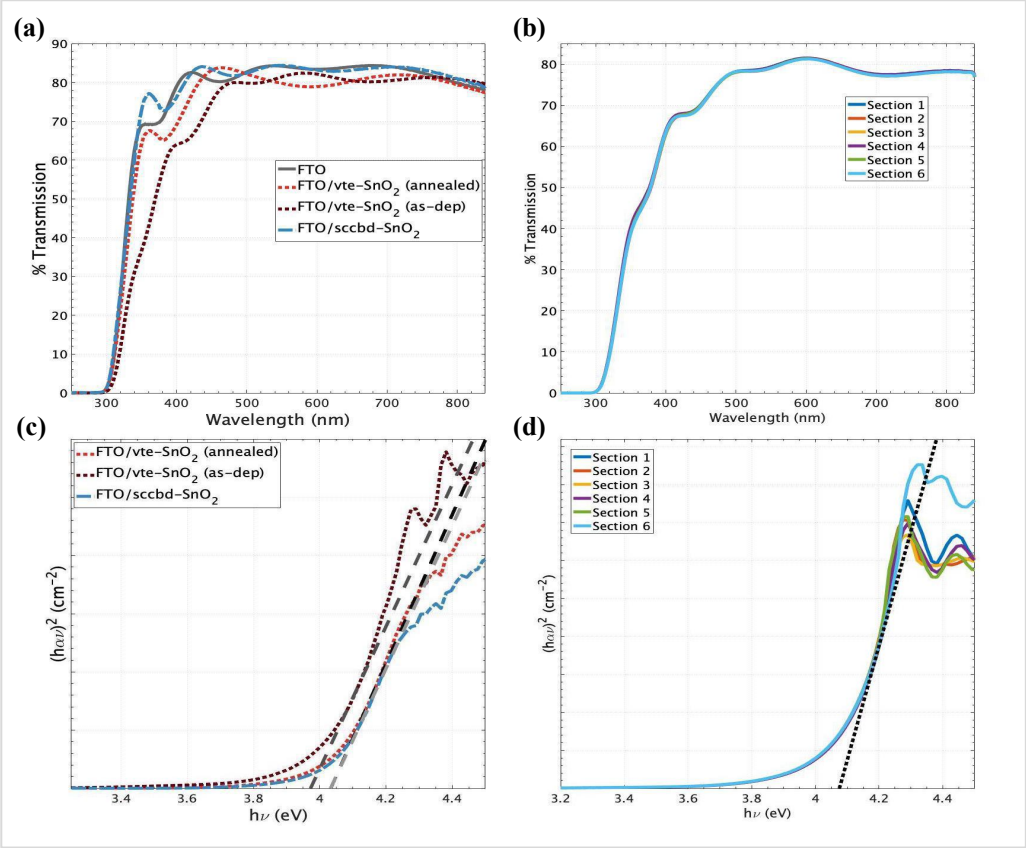

Figure 5.4: (a, c) UV-Vis transmission and Tauc plots for FTO, as-deposited vte-SnO_2, annealed vte-SnO_2, sccbd-SnO_2, and **(b, d)** for the six individual tested sections of the 100 cm^2 vte-SnO_2.

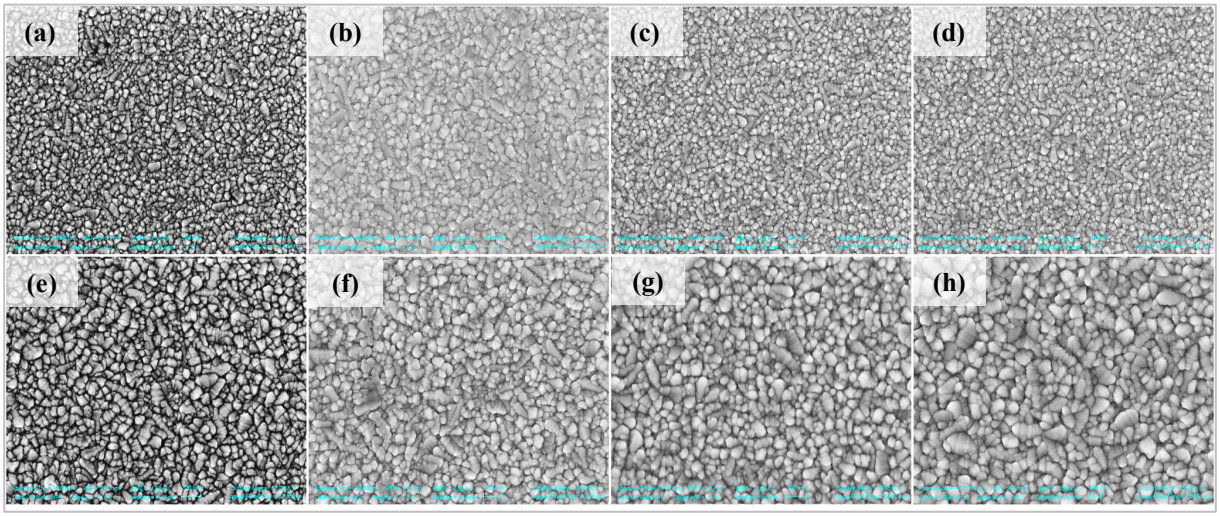

Figure 5.5: SEM micrographs of **(a, e)** FTO, **(b, f)** as-deposited vte-SnO_2, **(c, h)** annealed vte-SnO_2, and **(d, i)** sccbd-SnO_2. All micrographs are in relatively two different magnifications.

Taking a closer look with SEM to identify any micro-morphological differences reveals that all deposited ETLs resemble the underlying FTO substrate. The most noticeable difference can be seen on the as-deposited films, Figure 5.5b and Figure 5.5f where the irregular clumps of material with considerably different surface features are observed. The clumps are most likely formed from the physical nature of the vte deposition process and potentially result from vapor bursts or material agglomeration during condensation. Moreover, if these features are observed on the surface, they most likely occur throughout the bulk which would largely hinder device performance. After annealing, the surface features appear finer and the clumps are no longer observed.

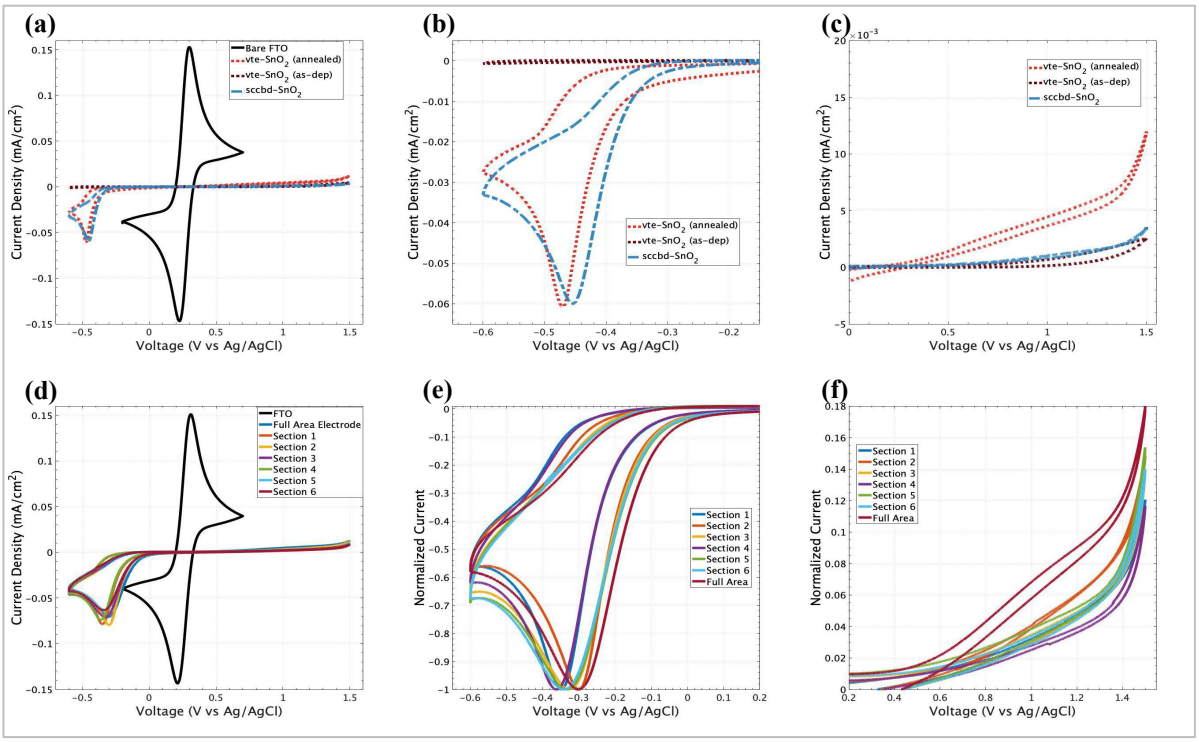

Figure 5.6: (a, b, c) Cyclic voltammograms of bare FTO compared to the as-deposited vte-SnO_2, annealed vte-SnO_2, and sccbd-SnO_2. **(d)** Cyclic voltammograms of the a 40 cm^2 FTO substrate, the vte-SnO_2 entire electrode, and for the six individual tested sections of the 100 cm^2 vte-SnO_2. **(e, f)** Corresponding cathodic and anodic peaks normalized to I_{max}.

To test the SnO_2 ETL surface coverage and rectifying CB behavior, CV measurements were performed in aqueous solution containing $Fe(CN)_6^{3-/4-}$ model redox couple. The $Fe(CN)_6^{3-/4-}$ redox potential of 0.24 V (vs Ag/AgCl sat'd) is sufficiently positive to the SnO_2 CB energy level and SnO_2 behaves electrochemically silent over the potentials analyzed. Therefore, all charge transfer prior to the rectifying CB edge is assumed to occur solely at the bare FTO surface. The complete suppression of redox couple peaks, compared to the bare FTO surface, confirms that the FTO surface is sufficiently covered. Full blocking of the $Fe(CN)_6^{3-/4-}$ charge transfer reaction occurs and only electron accumulation at the interface occurs until the bias has been raised to the CB energy, at which point $Fe(CN)_6^{3-}$ is reduced to $Fe(CN)_6^{4-}$. This rectifying behavior is not observed in the as-deposited vte-SnO2 and is likely the reason we are unable to extract current when incorporated in devices. Looking at Figure 5.6c it is clear that some FTO surface is revealed during the annealing process, most likely from cracking, but it is a negligible about and has not resulted in poor device performance. One thing to note is the more negative cathodic onset observed for the annealed vte-SnO_2 compare to the sccbd-SnO_2. The increased CB energy level is the proposed reason for higher V_{oc} is the solar devices discussed in later sections.[18,28]

5.3.2 ETL Influenced Absorber Characterization

Further characterization of the ETLs ability to extract charge from the perovskite layer can be assessed through photoluminescence (PL) intensity quenching. When charge carriers are excited to the CB, they can either recombine radiatively or non-radiatively. On an insulating substrate, like glass, the excited carriers are contained to the absorber and in theory all recombine radiatively producing high intensity PL signals. On an ETL, excited carriers near the surface recombine radiatively, while carriers near the ETL/perovskite interface ideally recombine non-

radiatively and are extracted due to the energetically favorable band alignment. Therefore, it is proposed that a reduced, quenched, PL signal is representative of an ETL's ability to effectively remove charge from the absorber. The large area point spectrum PL maps in Figure 5.7 are taken and then averaged to produce the spectra displayed in Figure 5.8. Although the sccbd-SnO_2 ETL displays higher quenching than the annealed vte-SnO_2, this does not necessarily mean that it is a better ETL. The degree of quenching is related to CB alignment, ETL conductivity, and interfacial contact. Both vte-SnO_2 (annealed) and sccbd-SnO_2 PL signals are adequately quenched, but the sccbd-SnO_2 signal is slightly higher. This presumably is from a larger CB energy offset between the perovskite and sccbd-SnO_2, which would be consistent CV results displayed in Figure 5.6b.

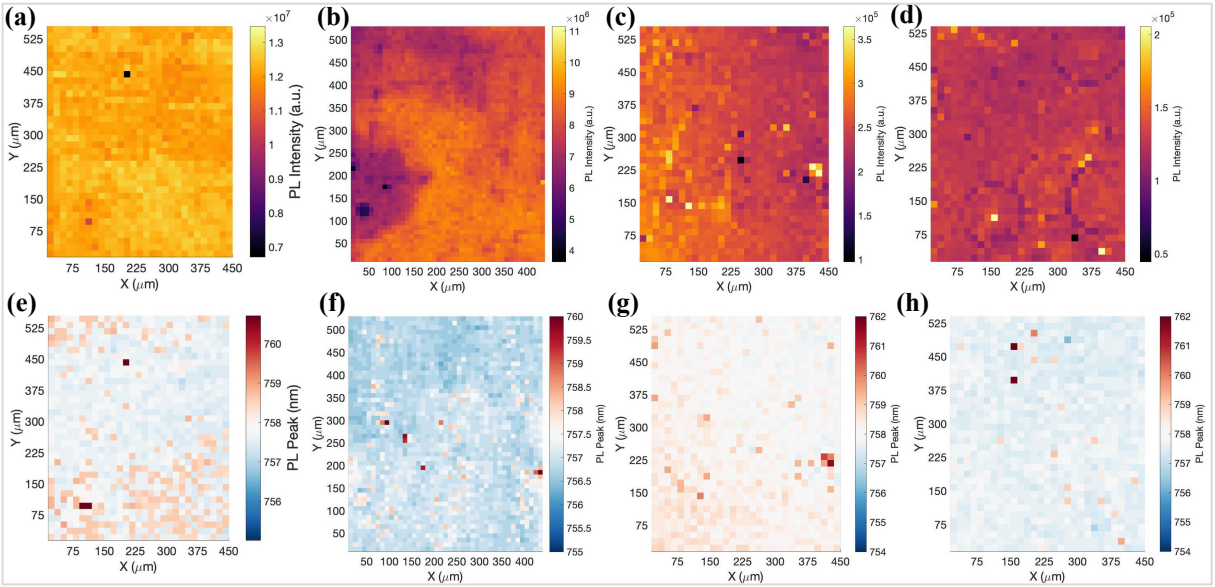

Figure 5.7: Steady-state photoluminescence maps of triple cation perovskite on **(a, e)** glass, **(b, f)** as-deposited vte-SnO_2, **(c, g)** annealed vte-SnO_2, and **(d, h)** sccbd-SnO_2. ETLs. The top and bottom rows correspond to the integrated intensity and peak wavelength at each point, respectively.

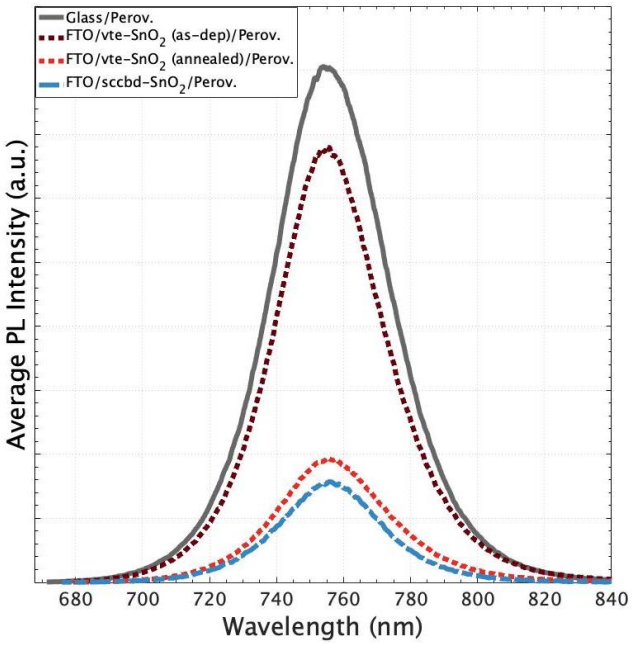

Figure 5.8: Average steady-state photoluminescence spectra corresponding to the mapped regions in Figure 5.6.

SEM micrographs were also taken of the triple cation perovskite atop the vte-SnO_2 and sccbd-SnO_2 layers to verify if there were any absorber morphological differences based on the underlying ETL. The individual grain features, ~200-300nm, that make up the film appear similar, but film wrinkling is observed on the vte-SnO_2. Wrinkling largely occurs to relive in-plane film stress during formation. Overall, the reports found that while wrinkling relieves film stress in the intermediate phase and determines film surface morphology, that final film stress is mainly determined by the annealing temperature and perovskite/substrate CTE mismatch. Most importantly, they report that the wrinkling does not alter performance, it just may be undesirable if a smooth surface is required.[33]

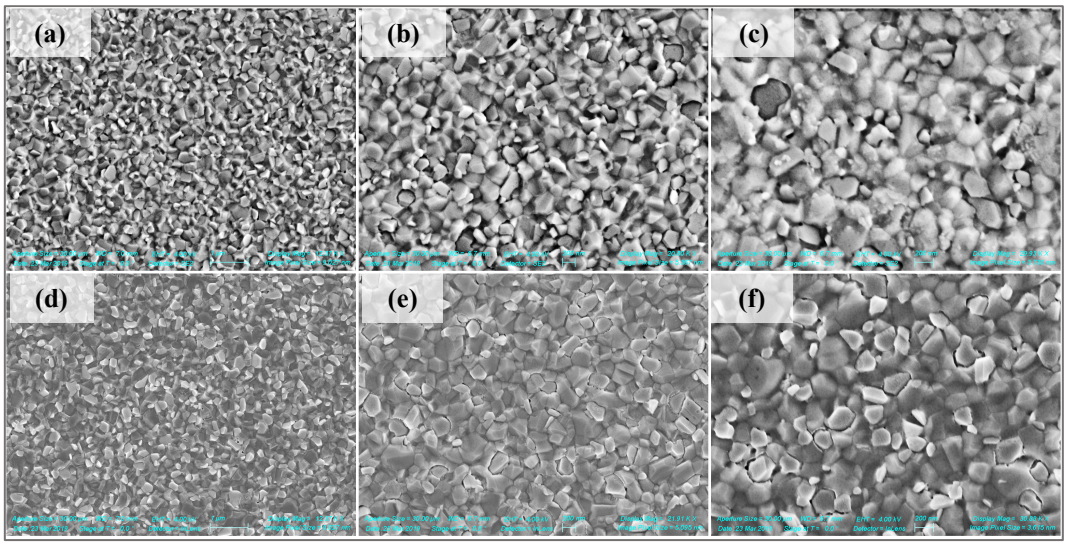

Figure 5.9: SEM micrographs of triple cation perovskite atop of sccbd-SnO_2 ETL. All images were taken using a secondary electron (SE) detector, however **(d, e, f)** were taken with an InLens SE detector.

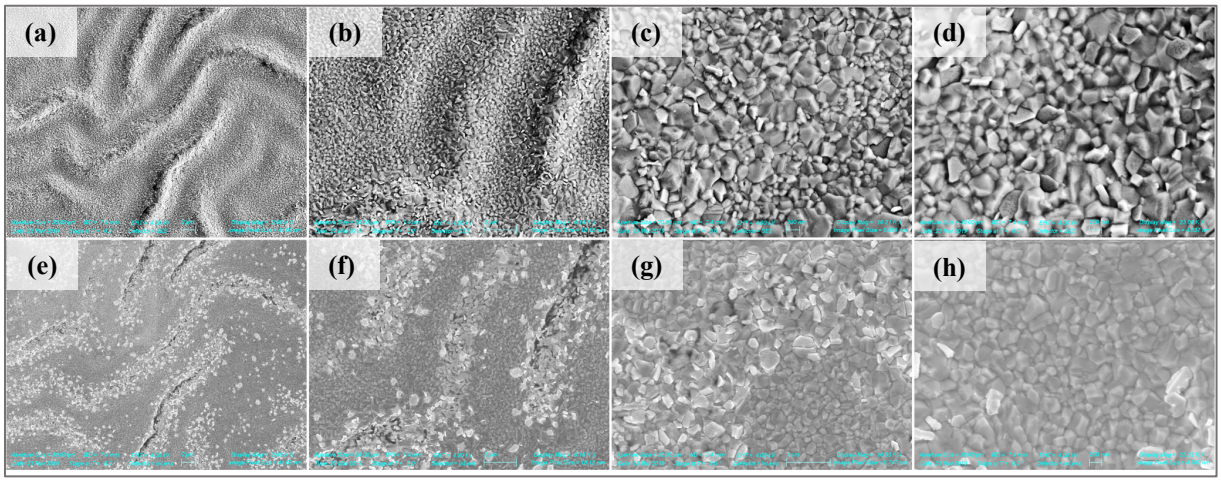

Figure 5.10: SEM micrographs of triple cation perovskite atop of annealed vte-SnO_2 ETL. All images are taken with primarily secondary electron (SE) detectors, however **(e, f, g, h)** were taken with an SE InLens detector.

5.3.3 *Device Performance*

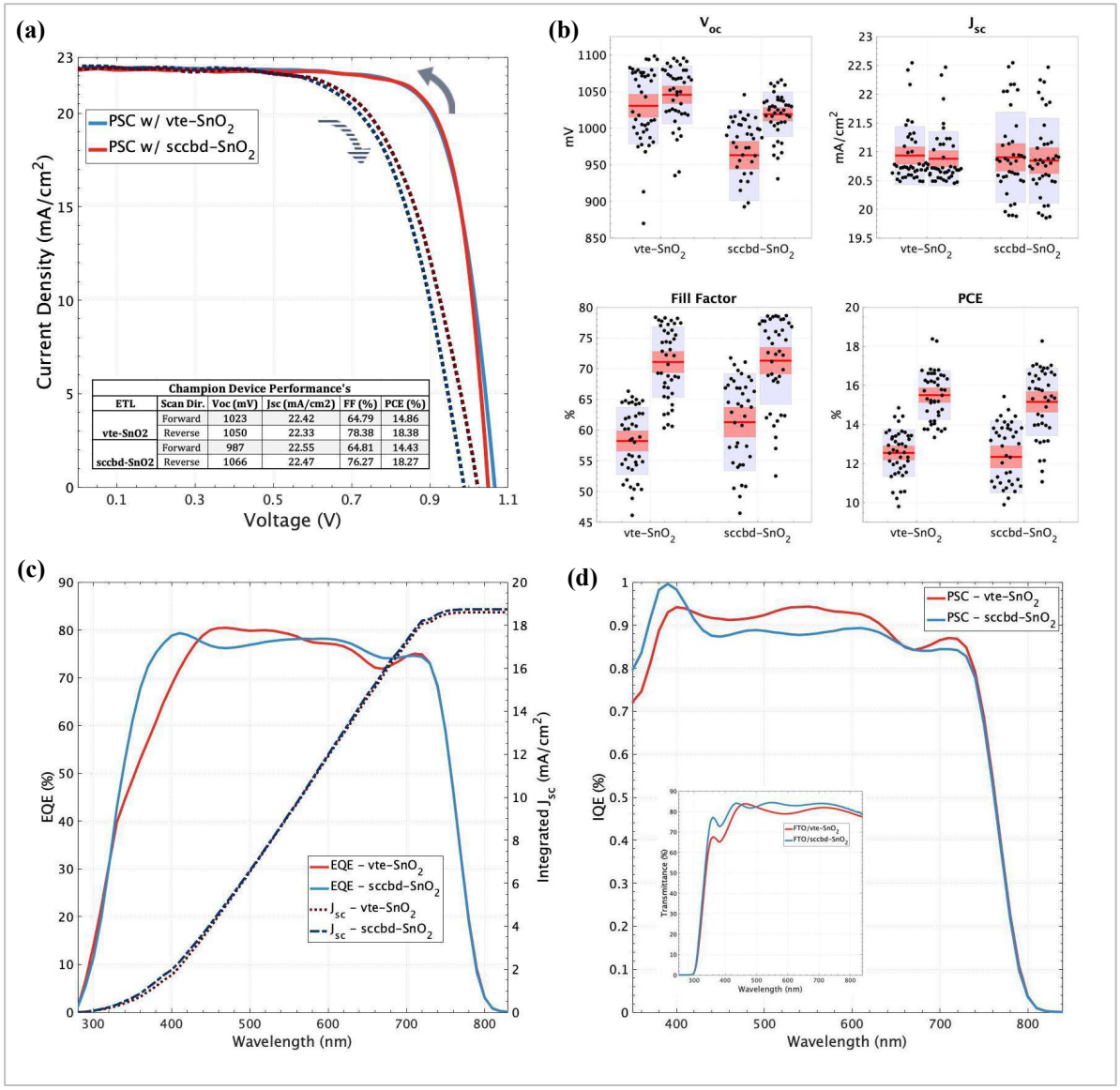

Figure 5.11: a) Champion IV curves and corresponding tabulated performance values. **b)** Overall performances for fabricated devices **c)** averaged EQEs and resulting integrated J_{sc}. **d)** Average IQEs with inset of transmittance curves used for calculation.

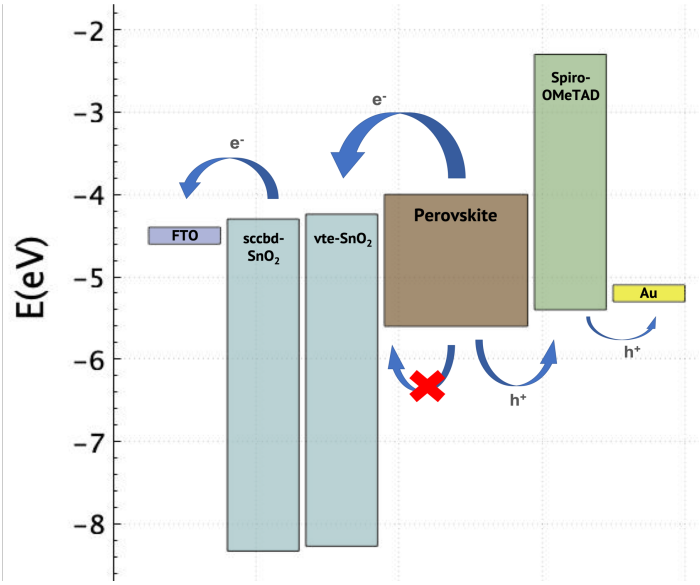

Figure 5.12: Proposed overall device alignment based on experimental data for the FTO, ETLs, and perovskite E_g, and literature values to fill in the rest.[34,35]

Champion IV curves displayed in Figure 5.11a, with PCEs of 18.4% and 18.3% for devices vte-SnO_2 and sccbd-SnO_2, respectively. Figure 5.10b displays box plots of the individual performances of 84 individual solar cells (42 with sccbd-SnO_2 and 42 with vte-SnO_2) fabricated under the same conditions. The collected data for each sample is divided into two sections corresponding to the forward, left, and reverse, right, scans. Furthermore, each box displays three highlighted values: the central red line represents the sample mean, the blue shaded box is one standard deviation, and the light right box illustrates the 95% confidence interval. Theoretically, a "true" sample mean doesn't exist since the goal is to continuously improve performance, but ideally the only variation between two sets is the ETL and we can compare the two populated sets of data. Under this assumption, some conclusions can be drawn based on the data presented in Figure 5.11 and the previously discussed thin film characterization. The first result is the apparent reproducibility in the vte-SnO_2 data. Even though a large amount of variation exists in the manufacturing process just based on day-to-day solution processing, the overall values are

more clustered than the sccbd-SnO_2 data. In regard to the ETLs' fabrication procedures, this consistency makes sense. The VTE procedure is automated, while the SCCBD procedure relies on an experimentalist every step of the way. The next point of interest is the higher V_{oc} observed in the vte-SnO_2 devices. This is consistent with the delayed cathodic onset potential observed in the CV data, pointing towards a higher CB energy level. Moreover, the average V_{oc} difference between the forward and reverse scan is much larger for the sccbd-SnO_2 devices, potentially resulting from a higher density of trap states at the interface. Moving to the top right of Figure 5.11b, devices with sccbd-SnO_2 display marginally higher average J_{sc}, most likely from the increased spectral absorption at bluer wavelengths. This trend is also observed in Figure 5.11c for the average EQE and integrated J_{sc}, but that's not to say that the vte-SnO_2 can't achieve the same current performance. Lastly, looking at the bottom right of Figure 5.11b, the average vte-SnO_2 PCE is slightly higher than the sccbd-SnO_2 PCE. This results from the higher consistency with the vte-SnO_2 device data. Although devices fabricated together typically have similar performance, devices with sccbd-SnO_2 often produce more low preforming outliers, which brings the average performance down.

5.4 Conclusion and Future Work

In conclusion, vte-SnO_2 is an effective method to produce large-area ETLs. The thermally evaporated layers can be used to produce highly efficient PSC devices reproducibly and with higher V_{oc} than the solution processed counter parts. The SnO_2 layer also displays almost no variation across a 100 cm^2 layer, useful for future module production. The future of this work should move towards developing a SnO_2 layer that requires no post-processing and can be deposited directly on top of the perovskite layer. This may be possible through installation of an

O_2 partial pressure feed either at the source for reactive evaporation or at the substrate to oxidize any alternative valence state Sn to Sn^{4+}. Moreover, this test would be relatively easily to perform without any device fabrication through UV-Vis transmission and CV characterization of the bare ETL layers. Furthermore, a gas feed could also prove useful depositing a NiO HTL, which is commonly vacuum deposited through reactive evaporation methods.

Chapter 6

Future Work in SnO_2 ETL Optimization and Hysteresis Reduction

6.1 Introduction

Throughout this work, various side projects were pursued to further enhance ETL properties or to better understand how ETLs impact overall device performance. The two projects discussed here are to serve as proof that the SnO_2 ETL CB edge contributes to V_{oc} pinning in Cs-doped triple cation PSCs and that interfacial traps are a main source for hysteresis in PSCs. The maximum achievable V_{oc} in a PSC is determined by intrinsic properties of the absorber. In PSCs with V_{oc}'s close to the achievable value are believed to have voltage losses due interfacial recombination. Therefore, the V_{oc} in these PSCs is largely determined by the quasi fermi-level splitting between the ETL's CB and HTL's VB; and deeper CB energies values will result in lower achievable device V_{oc}. Moreover, fabricating a full PSC device requires a great deal of time and resources. A full device stack requires 2 days more time than just synthesizing the SnO_2 ETL, in addition to, a spiro-OMeTAD HTL and Au contact, both of which are very expensive materials. The SnO_2 ETL and FTO contact layer are both relatively inexpensive and can be manufactured in a short period of time. The ability to optimize device V_{oc} performance without full solar cell fabrication would save time and resources. Here a correlation is proposed between ETL CV cathodic peaks and device V_{oc} that can potentially be used to maximize PSC performance.

6.2 Results and Discussion

Hysteresis is a commonly encountered issue in PSCs. There are a multitude of proposed reasons why this occurs, all of which have solid theoretical and experimental foundation. Hysteresis over time is believed to result from ion migration from the mobile halides ions in the absorber. Initial hysteresis on a primary IV scan however most likely result from the filling and emptying of interfacial trap states. Recent reports have indicated that by including potassium iodide (KI) in the perovskite may passivate intrinsic and interfacial traps states, and therefore reducing trap induced hysteresis.

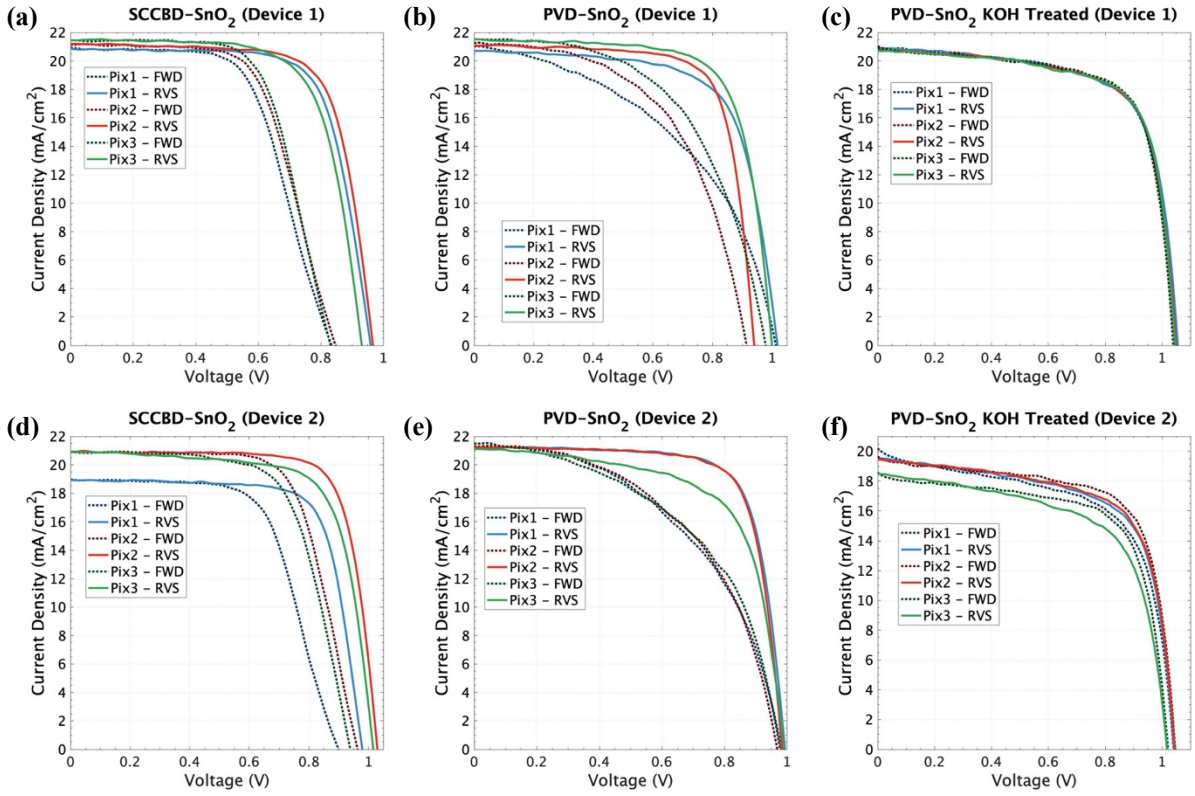

Figure 6.1: IV measurements PSC devices fabricated with **(a, d)** sccbd-SnO_2 **(b, e)** vte-SnO_2 and **(c, f)** KOH passivated vte-SnO_2.

In the figure above, the IV-curves in the rightmost section received a KOH surface passivation treatment to see if this reduced the observed hysteresis effect. It is clear that this treatment played a large role in reducing the observed hysteresis. Figure 6.1c displays a JV sweep from three solar cell devices on one substrate, all displaying the same efficiency in the forward in reverse direction. This does not commonly occur and is a quite remarkable result. The fact that not only the three cells have the same efficiency, but they have so for the forward and reverse sweep is a Below the overall performances are displayed for the JV sweeps in Figure 6.1. The more tightly clustered Fill Factor and V_{oc} aid more to the idea that this interfacial treatment worked in reducing hysteresis. These results illustrate a clear indication that interfacial traps play a large role in initial hysteresis observations.

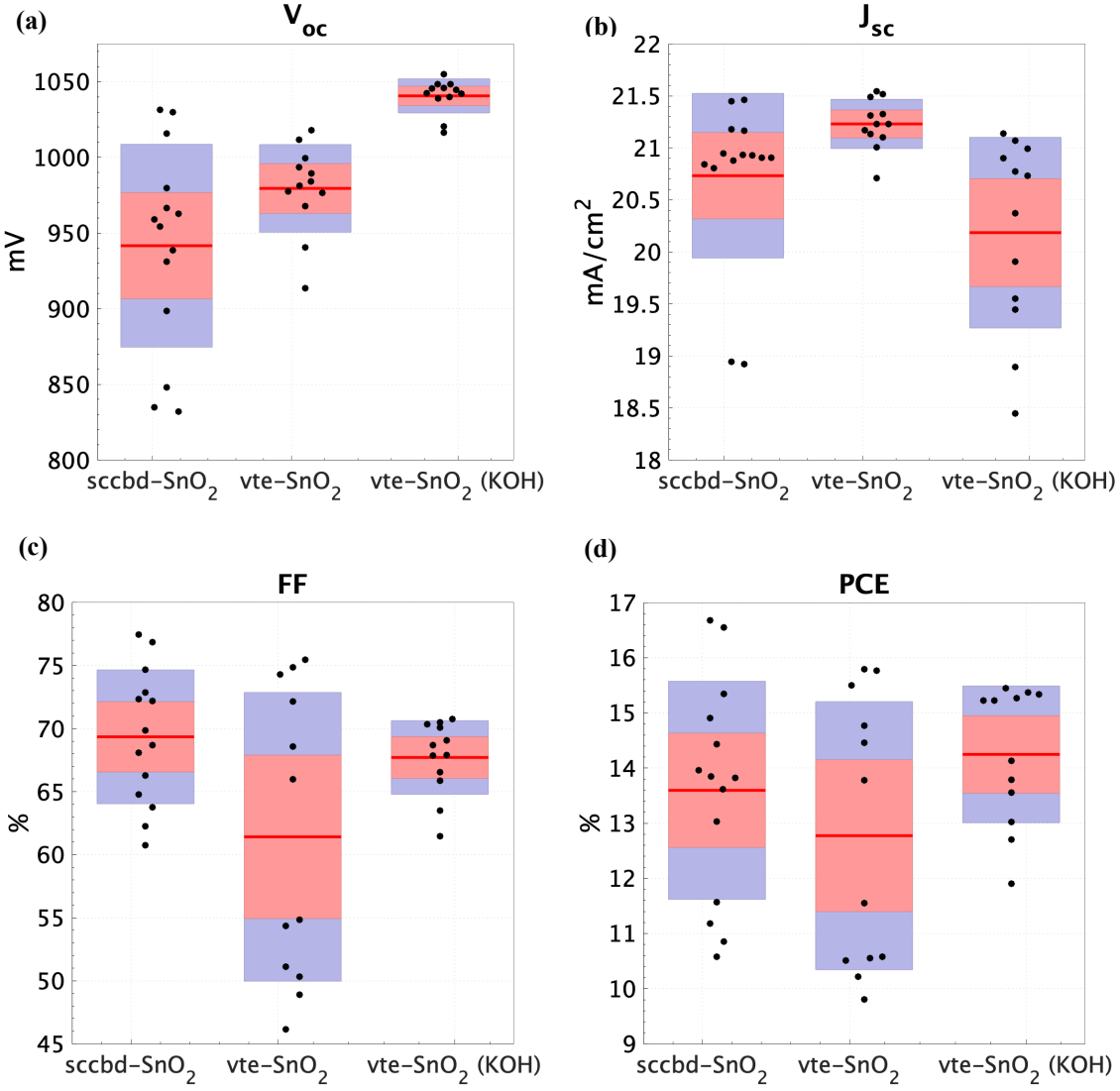

Figure 6.2: Overall IV performance metrics **(a)** V_{oc}, **(b)** J_{sc} **(c)** Fill Factor, and **(d)** PCE for the PSC containing sccbd-SnO_2, vte-SnO_2, and KOH passivated vte-SnO_2 displayed in Figure 6.1.

While the KOH treatment made it clear that interfacial traps lower the V_{oc} and result in hysteresis, it would be of great interest to identify this prior to fabricating a device. In metal oxide ETL research it is common practice to perform cyclic voltammetry measurements on the ETLs to ensure full surface coverage. The cathodic region of this experimental data should largely contain information about the SnO_2 CB edge and Fermi energy. Displayed below are four CV curves corresponding to four batches of vte-SnO_2. Since it is common practice to perform this measurement prior to device fabrication, one sample is removed from the whole fabricated set and tested. If the resulting CV curve indicates that the FTO surface is covered, the rest of the SnO_2 samples are moved forward with device fabrication or other forms of characterization. The Batch # corresponds to the SnO_2 batch fabricated on that given day. Further, the batches are not organized in chronological order, but to make the trend visually apparent in the succeeding analysis.

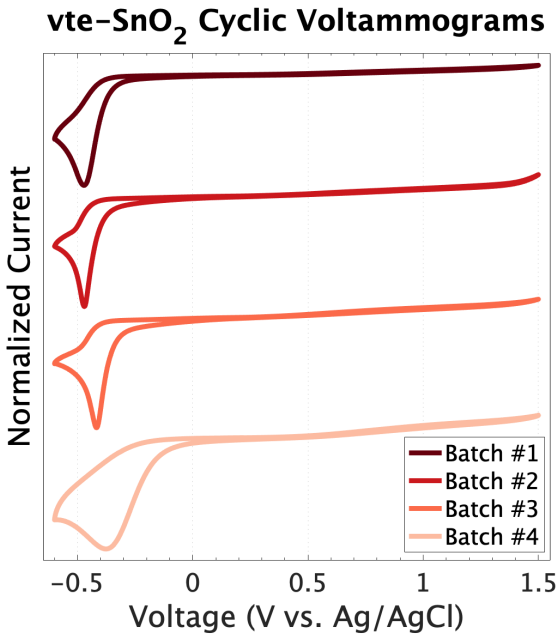

Figure 6.3: Cyclic voltammograms corresponding to four individual batches of vte-SnO_2. The curves have been normalized to the maximum current observed and stacked on top of each other

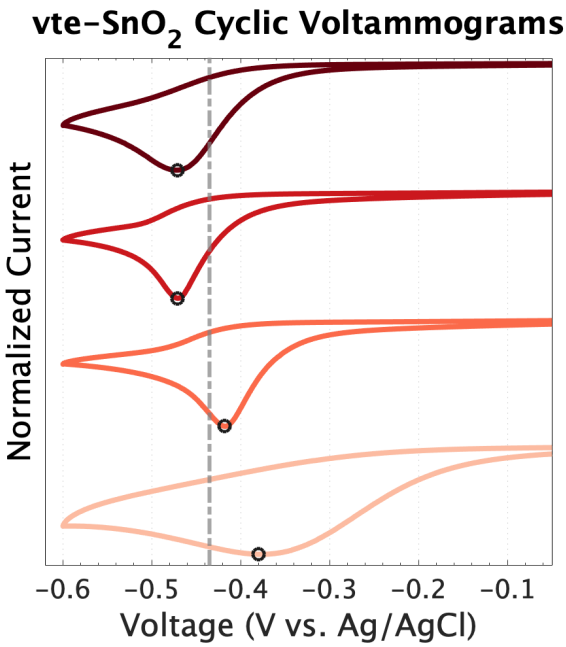

Figure 6.4: Cathodic region of cyclic voltammograms displayed in Figure 6.3. The voltage at the maximum current used to normalize the data is circled. These voltage values are used in the relation to device V_{oc}. The average of the four values is highlighted by the dashed grey line.

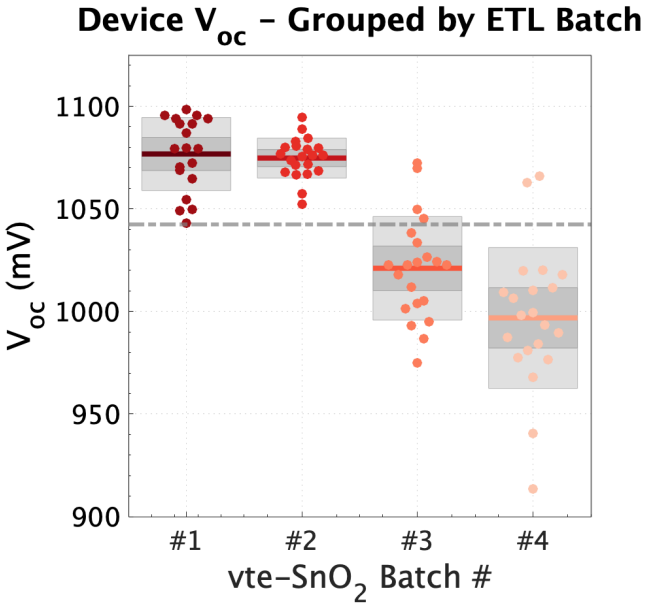

Figure 6.5: Device V_{oc} values separated by vte-SnO_2 ETL batch. The average of all V_{oc} values is highlighted by the grey dashed line.

Figure 6.4 shows the cathodic peaks zoomed in with the voltage at max current circled. The dashed line down the center the total average of the circled potential. Figure 6.5 then shows the resulting PSC device V_{oc}'s that were achieved with each batch of SnO_2. The dashed line down the center is the average of all the V_{oc} points displayed in the figure. The two sets were then plotted on the same graph with their averages tied to center of the corresponding y-axis and plotted over the same voltage range, $V_{avg} \pm 170$ mV. The clear trend between the two sets is extremely interesting and can prove insightful in ETL optimization.

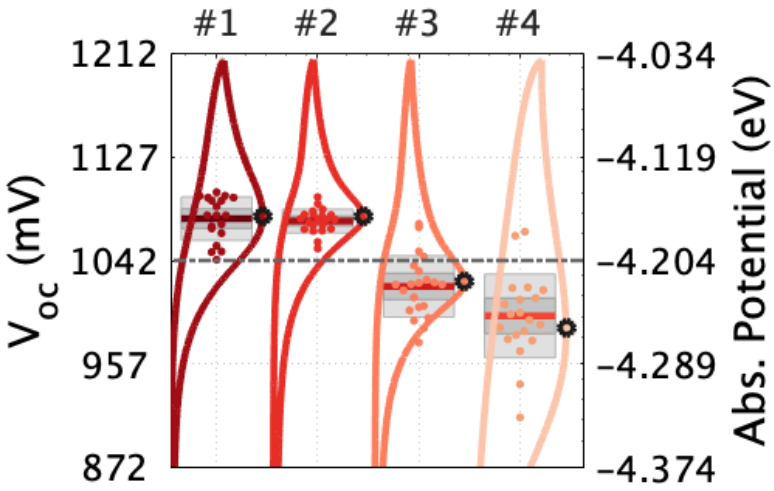

Figure 6.6: Data from Figure 6.4 and Figure 6.5 laid over each other. Both sets are plotted with their corresponding averages tied to the center over the same voltage range.

A fair deal of analysis can be performed with this data correlating the current to density of states and defect levels in the SnO_2 layers, however, Figure 6.6 alone speaks for itself. The relationship between ETL energy levels and device V_{oc} is obvious. Delayed voltage onset corresponds to higher CB and Fermi energy, which produces higher V_{oc}'s in PSC devices.

6.3 Conclusion and Future Work

In conclusion, promising initial experimental results illustrate the potential for PSC optimization through SnO_2 fabrication and characterization. The groundwork here is fundamental in illustrating that V_{oc} pinning is determined by transport layer properties and that initial hysteresis is largely a function of interfacial trap states. All in all, we can further improve Cs-doped triple cation PSCs through transport layer fabrication and interfacial trap recombination mitigation.

Appendix

Supplementary Information

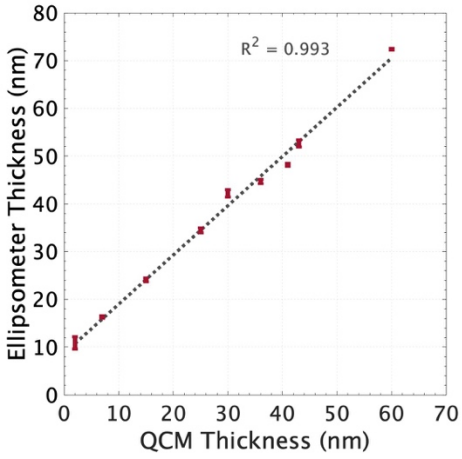

Figure S1: vte-SnO_2 QCM thickness calibration using ellipsometry. Samples were deposited on polished Si wafers and measured at various points across the substrate

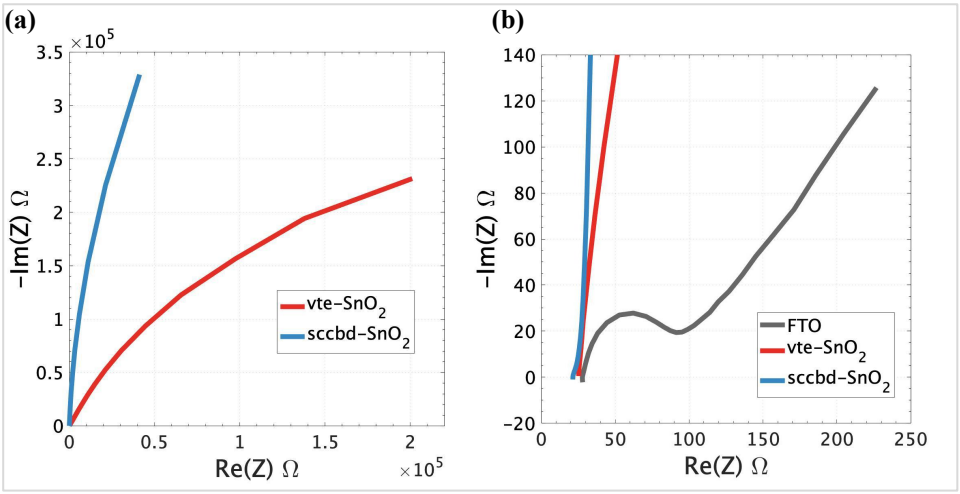

Figure S2: Electrochemical impedance spectroscopy at V_{oc} prior to CV measurements for **(a)** vte-SnO_2 and sccbd-SnO_2 compared to **(b)** FTO.

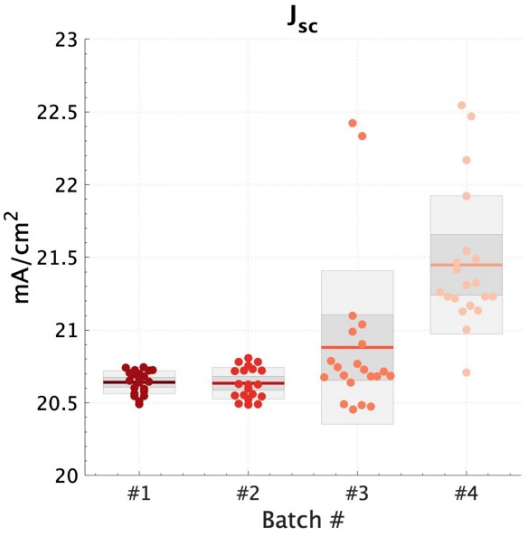

Figure S4: Short circuit current box plots corresponding to the PSC device performance separated by vte-SnO_2 batches.

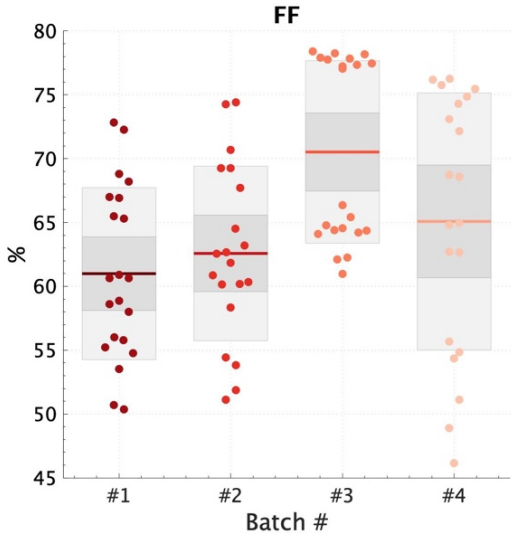

Figure S4: Fill Factor box plots corresponding to the PSC device performance separated by vte-SnO_2 batches.

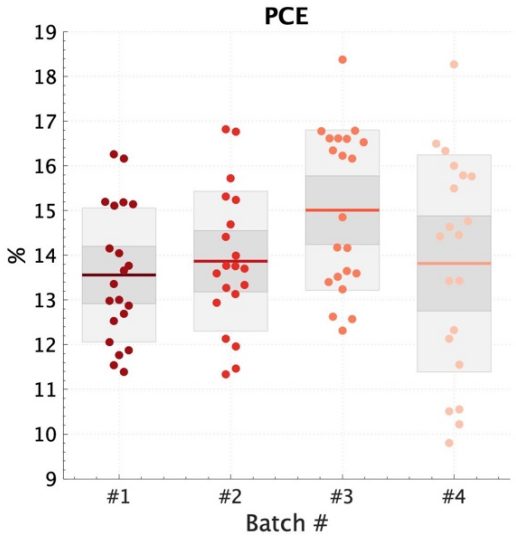

Figure S5: Power Conversion Efficiency box plots corresponding to the PSC device performances separated by vte-SnO_2 batches.

REFERENCES

(1) K. Jäger, “Solar Energy: Fundamentals, Technology, and Systems”. Delft University of Technology, 2014.

(2) M. Roser, E. Ortiz-Ospina, “World Population Growth”. 2019. url: https://ourworldindata.org.

(3) Department of Energy (DOE). “SunShot 2030”. 2019. url: https://www.energy.gov.

(4) National Renewable Energy Laboratory (NREL). “Best Research-Cell Efficiencies”. 2019. url: https://www.nrel.gov.

(5) N. T. Anh, “Atomic and Molecular Orbitals” in Frontier Orbitals, N. T. Anh (Ed.), 2007, pp. 5-24.

(6) A. Kamenko, T. Enriquez, M. Lam, “Quantum Numbers”. 2019. url: https://chem.libretexts.org.

(7) W. Locke, “Introduction to Molecular Orbital Theory”. 2019. url: http://www.ch.ic.ac.uk/vchemlib/course/mo_theory.

(8) P. Laube, “Semiconductor Technology from A to Z”. 2019. url: https://www.halbleiter.org.

(9) B. Van Zeghbroeck, “Chapter 2: Semiconductor Fundamentals” in Principles of semiconductor Devices.

(10) C. Cavallo, F. Di Pascasio, A. Latini, “Nanostructured Semiconductor Materials for Dye-Sensitized Solar Cells,” *Journal of Nanomaterials,* vol. 2017, 2017.

(11) Photovoltaic Education Network. 2019. url: http://www.pveducation.org.

(12) Photovoltaic Education Network. “Standard Solar Spectra”. 2019. url: https://www.pveducation.org.

(13) H. J. Snaith, “Perovskites: The Emergence of a New Era for Low-Cost, High-Efficiency Solar Cells,” *The Journal of Physical Chemistry Letters*, vol. 4, no. 21, pp. 3623–3630, 2013.

(14) “Perovskites and Perovskite Solar Cells: An Introduction”. 2019. url: https://www.ossila.com

(15) Z. Zhao, W. Sun, Y. Li, S. Ye, H. Rao, F. Gu, Z. Liu, Z. Bian, C. Huang, “Simplification of device structures for low-cost, high-efficiency perovskite solar cells,” *Journal of Materials Chemistry A*, vol. 5, no. 10, pp. 4756–4773, 2017.

(16) N. Marinova, S. Valero, and J. L. Delgado, "Organic and perovskite solar cells: Working principles, materials and interfaces," *Journal of Colloid and Interface Science*, vol. 488, pp. 373–389, 2017.

(17) Q. Wali, Y. Iqbal, B. Pal, A. Lowe, and R. Jose, "Tin oxide as an emerging electron transport medium in perovskite solar cells," *Solar Energy Materials and Solar Cells*, vol. 179, pp. 102–117, 2018.

(18) E. H. Anaraki, A. Kermanpur, L. Steier, K. Domanski, T. Matsui, W. Tress, M. Saliba, A. Abate, M. Gratzel, A. Hagfeldt, J.-P. Correa-Baena, "Highly efficient and stable planar perovskite solar cells by solution-processed tin oxide," *Energy & Environmental Science*, vol. 9, no. 10, pp. 3128–3134, 2016.

(19) L. Xiong, Y. Guo, J. Wen, H. Liu, G. Yang, P. Qin, G. Fang, "Review on the Application of SnO_2 in Perovskite Solar Cells," *Advanced Functional Materials*, vol. 28, no. 35, p. 1802757, 2018.

(20) Q. Jiang, X. Zhang, and J. You, "SnO_2: A Wonderful Electron Transport Layer for Perovskite Solar Cells," *Small*, vol. 14, no. 31, p. 1801154, 2018.

(21) M.F. Mohamad Noh, C.H. Teh, R. Daik, E.L. Lim, C.C. Yap, M.A. Ibrahim, N. Ahmad Ludin, Abd.R. bin Mohd Yusoff, J. Jang, M.A. Mat Teridi, "The architecture of the electron transport layer for a perovskite solar cell," *Journal of Materials Chemistry C*, vol. 6, no. 4, pp. 682–712, 2018.

(22) Q. Wali, Y. Iqbal, B. Pal, A. Lowe, and R. Jose, "Tin oxide as an emerging electron transport medium in perovskite solar cells," *Solar Energy Materials and Solar Cells*, vol. 179, pp. 102–117, 2018.

(23) E. Calabrò, F. Matteocci, A.L. Palma, L. Vesce, B. Taheri, L. Carlini, I. Pis, S. Nappini, J. Dagar, C. Battocchio, T.M. Brown, A. Di Carlo, "Low temperature, solution-processed perovskite solar cells and modules with an aperture area efficiency of 11%," *Solar Energy Materials and Solar Cells*, vol. 185, pp. 136–144, 2018.

(24) J. Ma, X. Zheng, H. Lei, W. Ke, C. Chen, Z. Chen, G. Yang, G. Fang, "Highly Efficient and Stable Planar Perovskite Solar Cells With Large-Scale Manufacture of E-Beam Evaporated SnO_2 Toward Commercialization," *Sol. RRL*, vol. 1, no. 10, p. 1700118, 2017.

(25) Y. Guo, X. Yin, J. Liu, W. Chen, S. Wen, M. Que, H. Xie, Y. Yang, W. Que, B. Gao, "Vacuum thermal-evaporated SnO2 as uniform electron transport layer and novel management of perovskite intermediates for efficient and stable planar perovskite solar cells," *Organic Electronics*, vol. 65, pp. 207–214, 2019.

(26) M. Saliba, J.-P. Correa-Baena, C.M. Wolff, M. Stolterfoht, N. Phung, S. Albrecht, D. Neher, A. Abate, "How to Make over 20% Efficient Perovskite Solar Cells in Regular (*n*–

i–p) and Inverted (*p–i–n*) Architectures," *Chem. Mater.*, vol. 30, no. 13, pp. 4193–4201, 2018.

(27) B. D. Viezbicke, S. Patel, B. E. Davis, and D. P. Birnie, "Evaluation of the Tauc method for optical absorption edge determination: ZnO thin films as a model system: Tauc method for optical absorption edge determination," *Phys. Status Solidi B*, vol. 252, no. 8, pp. 1700–1710, 2015.

(28) L. Kavan, N. Tétreault, T. Moehl, and M. Grätzel, "Electrochemical Characterization of TiO_2 Blocking Layers for Dye-Sensitized Solar Cells," *J. Phys. Chem. C*, vol. 118, no. 30, pp. 16408–16418, 2014.

(29) EC-LAB Software: Techniques and Applications. Version 10.38. BioLogic Science Instruments. 2014.

(30) J.A.N.T. Soares, "Chapter 2: Introduction to Optical Characterization of Materials" in Practical Materials Characterization. Springer Science and Business Media, New York, 2014.

(31) K.S.S. Harsha. Principles of Vapor Deposition of Thin Films. Elsevier Ltd. 2006.

(32) J. Wang, H. Li, S. Meng, X. Ye, X. Fu, and S. Chen, "Controlled synthesis of Sn-based oxides via a hydrothermal method and their visible light photocatalytic performances," *RSC Adv.*, vol. 7, no. 43, pp. 27024–27032, 2017.

(33) K. A. Bush, N. Rolston, A. Gold-Parker, S. Manzoor, J. Hausele, Z.J. Yu, J.A. Raiford, R. Cheacharoen, Z.C. Holman, M.F. Toney, R.H. Dauskardt, M.D. McGehee, "Controlling Thin-Film Stress and Wrinkling during Perovskite Film Formation," *ACS Energy Lett.*, vol. 3, no. 6, pp. 1225–1232, 2018.

(34) Z. Hawash, L. K. Ono, Y. Qi, "Recent Advances in Spiro-MeOTAD Hole Transport Material and Its Applications in Organic–Inorganic Halide Perovskite Solar Cells," *Adv. Mater. Interfaces*, vol. 5, no. 1, 1700623, 2018

(35) S. Weber, T. Rath, J. Mangalam, B. Kunert, A.M. Coclite, M. Bauch, T. Dimopoulos, G. Trimmel, "Investigation of NiOx-hole transport layers in triple cation perovskite solar cells," *Journal of Materials Science: Materials in Electronics*, vol. 29, no. 3, pp. 1847–1855, 2018.

(36) A. Mercurio, G. Horowitz, J. P. Gonzalez, and S. Almosni, "Impact of TiO2 electron transport layer properties on planar Perovskite solar cells," p. 49.

(37) Z. Li, H. Li, Z. Wu, M. Wang, J. Luo, H. Torun, P. Hu, C. Yang, M. Grundmann, X. Liu, Y. Fu, "Advances in designs and mechanisms of semiconducting metal oxide nanostructures for high-precision gas sensors operated at room temperature," *Mater. Horiz.*, vol. 6, no. 3, pp. 470–506, 2019.

(38) Y. B. H. Porte, “Investigation of intrinsic defects and versatility of Zn-doping in SnO2 thin films using pulsed laser deposition,” Imperial College London, Department of Materials. 2016.

(39) I. Concina, Z. H. Ibupoto, and A. Vomiero, “Semiconducting Metal Oxide Nanostructures for Water Splitting and Photovoltaics,” *Advanced Energy Materials*, vol. 7, no. 23, p. 1700706, 2017.

(40) M. N. Mullings, C. Hägglund, J. T. Tanskanen, Y. Yee, S. Geyer, and S. F. Bent, “Thin film characterization of zinc tin oxide deposited by thermal atomic layer deposition,” *Thin Solid Films*, vol. 556, pp. 186–194, 2014.

(41) R. A. Afre, N. Sharma, M. Sharon, and M. Sharon, “Transparent Conducting Oxide Films for Various Applications: A Review,” *Reviews on Advanced Material Science,* vol. 53, no. 1, pp. 79–89, 2018.